Title
ELEVATED TEMPERATURE COMBINED EROSION-CORROSION OF STEELS

Authors
Levy, A.
Slamovich, E.
Jee, N.

Publication Date
1985-04-01

Lawrence Berkeley Laboratory
UNIVERSITY OF CALIFORNIA

Materials & Molecular Research Division

Submitted to Wear

ELEVATED TEMPERATURE COMBINED
EROSION-CORROSION OF STEELS

A. Levy, E. Slamovich, and N. Jee

April 1985

Prepared for the U.S. Department of Energy under Contract DE-AC03-76SF00098

DISCLAIMER

LBL- 19156

ELEVATED TEMPERATURE COMBINED EROSION-CORROSION OF STEELS

Alan Levy, Elliott Slamovich and Nancy Jee
Lawrence Berkeley Laboratory
University of California
Berkeley, California 94720

Research sponsored by the U.S. Department of Energy under DOE/FEAA 15 10 10 0, Advanced Research and Technical Development, Fossil Energy Materials Program, Work Breakdown Structure Element LBL-3.5 and under Contract No. DE-AC03-76SF00098.

ABSTRACT

An investigation was made of the effect of erodent particle size and test temperature on the combined erosion-corrosion behavior of a series of chromium containing steels with 2 1/4,5,9, 12% and 18% chromium. The particle sizes used were 5μm, 50μm, and 100μm and the test temperatures ranged from 700° to 1000°C. The tests were made in the oxygen rich exhaust gases of a methane-air burner that propelled the particles at the specimens at 5 m/s for 30 minutes.

It was determined that corrosion was the dominant mechanism at all test conditions for all alloys. The erosion process enhanced the growth rate of multi-layered iron oxide and iron-chromium oxide spinel scales and markedly changed the morphology of the scale surface and the thickness of the various scale layers. These changes were determined to be affected by the particle size of the erodent, the test temperature and the chromium content of the alloy.

INTRODUCTION

The ability of steel alloy surfaces to withstand the combined degradation modes of erosion and corrosion at elevated temperatures is an important consideration in the design of emerging coal conversion and utilization systems. Processes such as coal gasification and fluidized bed combustion can impose harsh environments on metal containment surfaces. Separate studies of the corrosion and erosion of various alloys in environments partially simulating those that occur in process plants have been underway at this laboratory and several others for the past several years. Investigations of combined erosion-corrosion have also been conducted. The subject is an active research

area at the present time.

High temperature corrosion research in both oxidizing and reducing atmospheres, with and without the presence of sulfur in the corrodant gas to simulate coal reaction products, has determined the nature and rates of formation of oxide and sulfide containing scales on chromium containing steel alloys.[1-8] The effects of important variables such as chromium content of the alloy, exposure temperature and time, and the composition of mixed reactant gases on the morphology, composition distribution and rates of formation of scale products have been determined. The effects of coal char reactant products from coal gasifiers in contact with alloy steels on their elevated temperature corrosion rates and mechanisms have been determined for a number of different char compositions and exposure conditions.[9-11]

The erosion of metals in the absence of corrosion to determine the mechanisms of erosion have provided an understanding of how ductile metal surfaces deform and lose material from their surfaces.[12-15] Separate studies of the erosion mechanisms of the scales formed on the surfaces of metals at elevated temperatures prior to carrying out the erosion tests at room temperature have provided some insight into how brittle scales on ductile metals erode in both thick and thin layers. [16-17] Studies have also been undertaken to determine the behavior of alloys subjected to the combined effects of erosion and corrosion in a single test.[18-22]

Work in the field of erosion and corrosion has progressed to the point where observations of combined behavior can be partially interpreted in terms of the separate mechanisms which occur. In the

work reported in this paper, this background has been used in an attempt to gain a more basic understanding of what is happening and how the characteristics of the alloys tested and the test conditions combine to produce the degradation products that are observed. However, the unexpected results of combined erosion-corrosion reported herein raise many questions that cannot be readily answered from the foundation research that is referred to above. It is hoped that more detailed study and interpretation of the corrosion and erosion phenomina reported in the references and further research will result in more detailed understanding of the behavior that will be discussed below.

The test conditions used are representative of those which occur in the beds and free boards of fluidized bed combustors (FBC). The low velocity, 5 m/s, that was used is typical for a FBC as is the range of particle sizes, 5-100μm dia ave. Most erosion tests [1-8] use considerably higher velocities and generally, larger particle sizes. As such they are not as applicable to FBC tube erosion-corrosion as the investigation reported herein. The compromise that had to be made in this investigation was the test temperature for the alloys tested. While FBC's reach the test temperatures used, generally higher chromium content alloys are used at the higher test temperatures in FBC's.

TEST DESCRIPTION

The test specimens of each alloy (see Table 1 for composition) were exposed in the downstream duct of a methane-air burner operating with excess oxygen in the combustion gas. The exact partial pressure of

oxygen was not determined. The specimens were 1.25cm on a side cubes with a small hole through their center for mounting on an alumina rod that extended into the 10cm dia. duct perpendicular to its wall. The specimens were exposed so that two of their sides were at 45° angles to the exhaust gas and the other two sides were shielded from direct gas-particle impingement, thus providing two surfaces that were eroded-corroded and two surfaces that were only corroded on the same specimen. The ACES exhaust gas simulator at the Sandia Livermore National Laboratory Combustion Research Center was used for the tests. Figure 1 shows two test cubes in place on the rod with smaller alumina washer spacers between them during a test.

The test conditions were:

gas	oxygen rich methane-air combustion gas
velocity of particles	15 m/s
particles	5um dia coal ash ave
	50μm, 100μm dia Al_2O_3 ave
solids loading	6g/min
test duration	30 minutes
impingement angle	45°
specimen temperature	700°-1000°C
temperature differential across specimen	<6°C (measured by optical pyrameter during the test)

After the test exposure the specimens were cooled in less than 1 minute after the gas-particle flow was turned off by natural convection and radiation to temperatures <300°C where further corrosion could not occur, removed and the exposed surfaces and cross sections

microscopically analyzed using a scanning electron microscope (SEM) with KEVEX. Because different mechanisms occurred on the front (combined erosion-corrosion) and on the back (quasi-static corrosion) of each specimen at the same time, it was not possible to determine a degradation rate by either weight or thickness loss measurements.

RESULTS

Corrosion was the dominant mechanism of surface degradation at all of the test conditions investigated. The scales that formed and grew on the metal surfaces were affected by the impacting solid particles during their growth in several ways, depending upon the composition of the base alloy, the test temperature and the size of the erodent particles.

5μm Coal Ash Particles

The results of the tests that used 5μm dia, ave coal ash particles will be presented as a function of the chromium content of the alloys tested, starting with 1018 plain carbon steel with a 0% Cr content. Further, the results will be ordered by the test temperature, starting with the lowest temperature, 700°C. The patterns of behavior of the alloys appeared to follow these two variables in a somewhat orderly manner. The test temperatures, which ranged from 700°C for the 1018 to 1000°C for the 304SS, are generally above the top service temperatures of the various alloys tested. They were selected to achieve oxidation rates which could be readily studied after the short, 30 minute exposures in the burner duct. For all of the alloys tested, corrosion was the dominant mechanism.

1018

Figure 2 shows the surfaces of the corroded and the eroded-corroded sides of a single specimen after exposure to the oxygen rich, methane-air combustion gases and 5μm dia coal ash particles at 700°C. The observed surface on both sides consisted of iron oxide, Fe_2O_3.[6] The morphology of the scale on the corroded side consisted of a fine network of small needles with nodules of Fe_2O_3 penetrating up through them. A few coal ash particles from eddys in the flow behind the impingement sides of the specimen were also identified (the larger, light nodules). The eroded-corroded side had the same fine needle network as the corroded side, but the larger Fe_2O_3 nodules were not present. As can be seen, corrosion was the dominant mechanism on both sides. The fine needles that occurred on the eroded side did not appear to be vulnerable to the impact force of the impinging coal ash particles.

2 1/4CrlMo

Figure 3 shows the surfaces of this alloy after the 700°C test. The appearance of the surface is essentially the same as was seen on the 1018 steel specimen. Figure 4 shows the same alloy after the 800°C test. The morphology of both surfaces has changed somewhat. On the corroded side the Fe_2O_3 needles have formed into an interlaced network with some individual needles of larger diameter also occurring. Very few nodules of Fe_2O_3 are observed along with a very few coal ash particles (the larger, light grey particles in the lower photo).

On the eroded-corroded side, the morphology is somewhat different. The fine needle network appears to have condensed and a number of quite long comparatively large diameter, individual needles of oxide are seen growing out of the scale. Again, a few coal ash particles can be seen in the lower right photo. The delicacy of the long, individual needles on the eroded-corroded side is quite remarkable, considering that this side is being struck by coal ash particles. Note that the two lower photos are at the same magnification. The dynamic corrosion plus erosion that is occurring on the exposed side appears to be enhancing the growth of the oxide needles at this higher test temperature.

Figure 5 shows the SEM-KEVEX analysis of the surface scale on the eroded-corroded side of the specimen tested at 800°C. It can be seen that only iron oxide is present. The occurrence of only iron oxide on the surface with no chromium was observed for all of the alloys tested, except for the 304SS.

5Cr 1/2Mo

As the chromium content of the alloys increased the morphology of the oxide scale surface changed. The beginning of dramatic differences between the corroded side and the eroded-corroded side began with the 5Cr 1/2Mo Steel. Figure 6 shows the corroded (above) and eroded-corroded (below) surface at two test temperatures, 800°C and 875°C.

At the 800°C test temperature, the needle-like network of the scale can be seen on both the corroded and eroded-corroded sides. A few nodules appear on the corroded side; none on the eroded-corroded side. The same thing occurred on the 1018 and 2 1/4Cr1Mo steels at the lower, 700°C temperature (Figures 2 and 3). It appears that test

temperature and chromium content trade off in the resultant oxide structures. As the chromium content increases, the surface morphology reverts back to that which occurred in the lower chromium content alloys at lower test temperatures.

At the 875°C test temperature, the next major change in the morphology occurred. The needles are almost non-existent on the corroded side (upper right photo) and they are replaced by nodules and columns of Fe_2O_3. The columns are different from the nodules in that their tops appear to be somewhat pointed and porous or wrinkled on the corroded side. The great difference in the morphology between the corroded and eroded-corroded sides first occurs on the eroded-corroded surface of this alloy. It consists entirely of crystalline columns of significantly greater cross section than the pointed-porous topped columns on the corroded side and their tops do not show any porosity. This behavior was observed on the higher chromium content alloys at higher test temperatures to an even greater degree, as will be seen.

9Cr1Mo

Figure 7 shows the extent to which the great difference occurred in the morphology of the 9Cr1Mo steel between the corroded and eroded-corroded sides of the same test specimen. On the left side of the figure is the corroded side with a myriad of small diameter pointed-porous or wrinkled topped columns extending up perpendicular from the metal surface. The few gray globules are coal ash particles. On the right photo is the eroded-corroded surface. The well defined crystalline columns of iron oxide (no chromium was determined) are many

times the size of the columns on the corroded side and are no where near as numerous. Many of their tops have been chiselled away to form more or less points and no porosity or wrinkling can be observed at the tops of the columns. The action of the eroding coal ash particles can be seen to affect individual columns, but do not result in an overall eroding away of the surface. The relatively low density of the columns and their large size seems to reflect a selective thinning of the columns compared to the density of those that occurred on the corroded only side so that the remaining columns could grow to a much larger size. This phenomenon appears to be similar to the selective thinning of trees in a forest to promote the growth of the remaining ones.

The determination of the composition of the columns on both the corroded and eroded-corroded sides of the 9Cr1Mo steel specimens was made by SEM-KEVEX analysis. Figure 8 shows the analyses of the scales that formed on the 9Cr1Mo steel. It can be seen that both types of columns are iron oxide with no chromium present. The presence of some coal ash is shown by the presence of such elements as Si, Ca, Al and Mg. The reason that the corroded side has more coal ash present is that the velocity of the particles on the back side of the specimens in the flow eddy is much slower than on the front side that directly receive the impact of the coal ash at the full 5 m/s. The wafting particles on the back side can more readily get caught in the forest of columns that exists there.

The effect of test temperature on the morphology of the scales formed on the 9Cr1Mo steel are shown in Figure 9. On the left side are shown the surfaces after the 800°C test. Essentially the surface is a

continuous Cr_2O_3 scale with some nodules of Fe_2O_3 and a few coal ash particles on the surface. The eroded-corroded side shows a slightly eroded Cr_2O_3 surface. At this lower temperature, compared to the 950°C exposed specimen shown in Figure 8, the chromium is present in sufficient quantity to form a typical protective barrier-type scale. The eroded-corroded side is still a mild enough overall condition to enable the alloy to maintain the protective scale.

When the test temperature is increased to 950°C (photos on the right side of Figure 9) the same type of behavior as was shown in Figure 7 is evident. In Figure 9 the magnification is higher than in Figure 7 and the nature of the columns can be more readily seen. Also, in the lower right photo another aspect of the erosion process is shown. In some isolated areas the columns had been eroded away, leaving a more continuous scale showing beneath them. The contours appearing on the scale layer is direct evidence of the erosion process. The overall differences between the surface morphologies of both the corroded and eroded-corroded sides of the specimens at the two test temperatures are pronounced.

410SS

The 410SS specimens showed the same type of behavior as the lower chromium content, ferritic steels that formed columns. Figure 10 shows the two surfaces after testing at 950°C. The chiselled tops of the eroded-corroded side columns toward pointed shapes are clearly evident as are their greatly increased size over the corroded side columns. Note the difference in magnification at both the lower and the higher magnifications. At least one of the columns (lower right side photo)

is cracked, providing a short circuit diffusion path.

It is possible that the large diameter, dense columns that form on the eroded-corroded side could retard metal loss once they form. The basis for the retardation of metal loss is contained in Reference 16 where it was reported that dense, columnar NiO scale on a nickel substrate eroded at substantially lower rates than equiaxed, porous NiO. On the other hand, the voids between the large columns and the increased diffusion rates in the dense columns could enhance corrosion and scale formation.

Figure 11 shows the SEM-KEVEX peak analyses. Even with 12% Cr content in the alloy, the columns of oxide at the surface were determined to be iron oxide with no chromium. It is interesting to note, however, that the No. 2 peak on the eroded corroded side shows some chromium in a crystallite that appears to be below the general level of the columns. Some coal ash was retained on the corroded side of the specimen, peak 2, where the velocities are very low. The coal ash is composed of oxides of magnesium, aluminum, silicon, potassium and calcium as well as some additional, minor oxides and sulfides. Coal ash is known to be corrosive of itself. The ash particles are slowed down considerably in the wakes on the back sides of the specimens and can get caught in the columns of scale.

The 410SS specimens were cross sectioned to determine the nature of the scale down to the base metal. Figure 12 shows the morphology of the scales and the distribution of iron and chromium through them. Analysis of the photos indicates that combined erosion-corrosion not only changes the surface morphology of the scale compared to straight

corrosion, but also the cross section morphology and composition.

On the corroded side (left side photos) the secondary electron image indicates that there is a duplex scale present with a line of porosity separating the two phases. Analyzing the x-ray maps shows that the top layer is iron oxide with no chromium in it, as has been discussed above. However, the second layer of the scale has substantial chromium content and is either Fe_2O_3 with chromium dissolved in it or an iron-chromium oxide spinel.[6] This layer has a scalloped, intimate bonded interface with the base metal. The cross sections of the small, pointed columns of surface scales described earlier can be readily seen in the upper left photo.

The morphology of the scale cross section on the eroded-corroded side of the specimen (right side photos in Figure 12) is quite different from that on the corroded only surface. The surface of the eroded-corroded side is made up of relatively large diameter columns of Fe_2O_3 with void areas between them that extend down to the iron-chromium oxide layer. It is for this reason that there is a chromium peak in Figure 11 on the eroded-corroded side. The cross sections of the columns on the surfaces of the corroded and eroded-corroded sides of the same specimen verify the observations made earlier concerning the morphological differences between the surfaces of the corroded and eroded-corroded scales.

Referring to the x-ray maps, it can be seen that the scale thicknesses of each of the constituents on the corroded and eroded-corroded sides as well as the distribution of the two phases on each side are markedly different.

On the corroded only side of the specimen, both the Fe_2O_3 and iron-chromium oxide layers have approximately the same thickness. The contact area between the lower scale layer and the substrate metal is intimate with no voids present. The outer, Fe_2O_3 scale is much thinner on the erosion-corrosion side, extending only to the base of the columns. The Fe-Cr oxide layer is much thicker on the eroded-corroded side, essentially constituting the main body of the scale. Also, the interface between the lower layer of the duplex scale and the base metal is quite porous on the erosion-corrosion side. The large increase in the iron-chromium oxide layer thickness apparently has depleted the substrate surface in chromium sufficiently to cause some Kirkendall type voids to occur at the scale-metal interface. The amount of voids between the upper and lower scales is near the same for both sides. Thus the occurrence of erosion in conjunction with corrosion, with the corrosion process dominant, changed the morphology and the composition distribution of the scale that was formed.

304SS

The 304SS, an austenitic alloy with a significantly higher chromium content than any of the chromium containing ferritic alloys tested, behaved in a somewhat different manner than the other steels at temperatures higher than were used to test the other steels but still using 5μm coal ash particles. Figure 13 shows that the surfaces developed a continuous Cr_2O_3 scale on both the corroded and eroded-corroded surfaces and that the barrier scale was not penetrated by the eroding particles.

On both the corroded and eroded-corroded surfaces, nodules of iron-chromium spinel have penetrated up through the Cr_2O_3 scale layer. The size of the nodules is considerably larger on the erosion-corrosion surface than on the corroded surface. This follows the general trend throughout the test series of having combined erosion-corrosion enhance the growth of individual crystallites on the scale outer surface. Some of the nodules present on the surface are coal ash.

Laser Raman spectroscopy was used to identify the phases that were present on the surface of the 304SS test samples. Figure 14 shows the Raman spectra for the corroded surface. The peak at 570 is Cr_2O_3, the peak at 660 is spinel and the small peak at 1010 represents the compounds in coal ash. Figure 15 shows the Raman spectra of an area on the surface of the eroded-corroded side. The additional peaks over and above those that occurred in Figure 14 are due to coal ash particles adhering to the surface. These spectra indicate that individual nodules of iron-chromium oxide spinel formed on the iron-chromium-nickel 304SS rather than the iron oxide nodules that formed on the straight iron-chromium alloys.

Effect of Particle Size

In order to determine what type of scale morphology would occur on the eroded-corroded surfaces when larger eroding particles were used which could transfer a greater force to the surface upon impact, 50μm and 100μm Al_2O_3 particles were used to erode 410SS. All of the other test conditions were the same as were used in the 5μm coal ash tests. It was thought that while the small, 5μm coal ash particles used in the earlier tests were too small to result in erosion being the dominant

mechanism, the larger particles could change that circumstance.

As the particle size of the erodent increased, major changes occurred in the morphology of the iron oxide scale surface. Figure 16 shows the surfaces of the erosion-corrosion side of 410SS eroded by 5μm flyash and 50μm and 100μm Al_2O_3. As the particle size increased from 5μm to 50μm diameter particles, the diameter of the iron oxide columns decreased and the number increased. The type of column caused by the 50μm particles reverts to that which occurred on the corrosion side of the specimens in the 5μm flyash test, Figure 10. A further increase in particle size to 100μm diameter Al_2O_3 caused a further major change in the topography of the scale surface, as can be seen in the lower photo in Figure 16. There are a minimum number of small nodules rising out of a cracked continuous iron oxide scale layer.

The variation in surface morphologies as a function of erodent particle size followed a pattern found in all of the other chromium containing steels tested. For example, Figure 17 shows the effect of erodent particle size on the surface scale morphology of the 5Cr 1/2Mo steel. Note that the magnification of the scale on the 100μm Al_2O_3 is one-third that of the two photos above it. A major change in the diameter and shape of the needles or blades formed on the erosion-corrosion surface occurred between the 5μm flyash and the 100μm Al_2O_3 tests. The 50μm diameter particles resulted in a surface morphology that was similar to that found on the 410SS when it was eroded with 50μm diameter particles, see Figure 16. This small diameter column morphology was found on almost all of the alloys that were eroded with 50μm diameter particles.

The cross sections of scales on two alloys with significantly different chromium contents from tests using 100μm diameter Al_2O_3 particles are shown in Figures 18 and 19. The scales were still multi-layered but differed significantly from those which occurred when 5μm flyash was used. It can be seen that the overall thickness of the scale on the eroded-corroded side of both the 2 1/4 CrlMo steel (Figure 18) and 410SS (Figure 19) specimens is much greater than that which formed on the corrosion only side of the specimens (note the differences in magnification of the photos). The erosion process markedly enhanced the growth of the scale.

Figure 18 shows the cross sections of the scales formed on the much lower chromium content 2 1/4 CrlMo steel when 100μm particles were used at a lower test temperature than was used for the 410SS. The scale is essentially iron oxide. The chromium has concentrated in a thin iron-chromium oxide spinel layer at the scale-metal interface. The scale on the eroded-corroded side is significantly thicker than that on the corroded side, as occurred on 410SS. The scales that formed on both sides of the specimen were almost completely separated from the substrate, indicating a strong suceptibility to spalling.

The distribution of the iron oxide and iron-chromium oxide scale layers on the 410SS was changed between the eroded-corroded scale in the 5μm flyash test, Figure 12, and the 100μm Al_2O_3 test shown in Figure 19. The iron oxide, upper layer, is now the thicker layer with not as much iron-chromium oxide spinel forming, relatively, as occurred in the 5μm flyash test. Small diameter voids occurred throughout the scale layers on the eroded-corroded side but did not occur on the much

thinner scale on the corroded only side.

There is also an internal scale layer that has formed on the eroded-corroded side, below the voids at the scale-metal interface that does not contain chromium. Based on evidence in Reference 7, it is probably inward growing Fe_3O_4 . The much smoother surface of the 100μm particle test scale compared to the 5um particle test scale is also indicated in Figure 19.

The consistent effect observed on all of the alloys for the eroding particles to increase the scale thickness on the erosion-corrosion side of the test specimen compared to the corrosion only side was checked against the dynamic corrosion obtained by testing specimens in the flowing gases of the ACES burner without injecting any particles. Figure 20 compares the scales formed and their thicknesses for a number of test conditions. It can be seen by comparing the top two photos that static corrosion on the back side of the specimen and dynamic corrosion on the front side (gas flow without particles) results in nearly the same scale thickness with approximately a 10% increase on the dynamic corrosion side. This compares with a 60% increase in the scale thickness on the erosion-corrosion side when 5μm particles are used and a 345% increase when 100μm particles are used, all compared to the static corrosion only side scale thickness.

Cross sections of the erosion-corrosion scales are seen in the lower two photos in Figure 20. While the morphology of the static and dynamic corrosion scales are similar, there is a major difference in the two eroded-corroded scales in addition to their thickness difference. This seemingly anamolous behavior of the more erosive

(larger size) particles causing markedly thicker scales to form was consistently observed for all of the chromium containing steels tested.

The differences in the morphology of the cross section and surface of three of the chromium containing steels tested at the same conditions are shown in Figure 21. These steels were eroded by 100μm Al_2O_3 particles. All three had iron oxide outer scales with the two higher chromium content steels having sizeable inner scales of iron-chromium oxide spinel.

The character of the surface of the outer scale differed for the three steels. The large, light particles on the surface of the 2 1/4Cr1Mo steel are alumina erodent particles that became embedded in the iron oxide scale. Note the difference in magnification between the three photos on the right side of Figure 21. The rosettes of iron oxide that formed on the 9Cr and 12Cr steels are completely different from the iron oxide morphology on the 2 1/4Cr1Mo steel. The rosettes on the 410 steel are much larger than those which formed on the 9Cr1Mo steel (note the difference in magnification between the two photos). Similar rosettes of oxide scale are shown in Reference 8.

In contrast with the differences in the eroded-corroded surfaces that were shown in Figure 21 when the erodent was 100μm Al_2O_3 the use of 50μm Al_2O_3 erodent particles resulted in a very similar surface scale morphology for the three alloys of varying chromium content shown in Figure 22. The columns of iron oxide with wrinkled and porous tops are similar in size and shape to the corroded only side of the 410SS specimen that was tested with 5μm flyash, see Figure 10. The scale morphologies of the three alloys shown in Figure 22 are completely

different from their eroded-corroded surfaces when tested using either 5μm or 100μm size particles, see Figure 10 and 21. The cross sections of the three scales are multi-layered and have generally similar morphologies. The scale thickness of the 9Cr and 12Cr steels was thinner when the 50μm particles were used than when the 100μm particles were used as can be seen by comparing Figures 21 and 22 (note magnification differences).

Effect of Temperature

The morphology of the surface iron oxide scale was also affected by the test temperature when 5μm flyash and 100μm Al_2O_3 erodents were used, but not when 50μm Al_2O_3 particles were used. Figure 23 shows the changes that occurred on the 9Cr1Mo steel specimens when the temperature was changed from 800° to 950°C and 100μm size particles were used. The large diameter needles or blades that grew at 950°C were very similar to those which grew at 800°C on the 5Cr1/2Mo steel shown in Figure 17. The increase in the size of the microstructural elements with increasing temperature was expected, but the delicacy of some of the iron oxide crystals on surfaces that were being impacted by 100μm size particles as they were growing was unexpected.

Figure 24 shows the surfaces of the same alloy, 9Cr1Mo steel, at three different test temperatures when 50μm Al_2O_3 particles impacted the surface. As in the case of varying the chromium content shown in Figure 22, varying the test temperature resulted in essentially the same type of microstructure for all three temperatures. The morphology was the same wrinkled, porous topped columns that were shown in Figure 22.

The effect of test temperature on the surface morphology of the alloys tested with the 5μm flyash particles was generally more dramatic in the differences that occurred. Figure 25 shows the surface of 410SS tested at 850° and 950°C on both the corroded and eroded-corroded surfaces. At the lower test temperature on the corroded side, some of the needle type crystals observed on the surface of the lower chromium content steel occurred. On the eroded-corroded side at the 850° test temperature, the needles have been removed and the remaining structure is essentially unaltered. Increasing the test temperature by 100°C markedly changed the morphology of the surface of the iron oxide on both the corroded and eroded-corroded surfaces as can be seen on the right side photos in Figure 25.

DISCUSSION

Qualifications

The major changes in the surface and cross section morphologies and compositions of the iron oxide base scales that formed on the chromium containing steels were unexpected. While there is some work in the literature that analyzes the growth of iron oxide and iron-chromium oxide spinels on the surfaces of chromium containing alloys, [6,8] the gross changes in morphology that were observed in this work, especially those that were promoted by the erosion process, have not been reported previously. Studying the high temperature corrosion literature referenced in the introduction only begins to account for the behavior reported therein.

Much work of interpretation and determination of mechanisms of the scales that formed must still be done. Hence, this discussion of the

observed behavior will not be in depth at this time. Primarily, the work to date has identified phenomina that require more work to explain adequately.

The predominance of corrosion over erosion on the surfaces of ferritic steels with chromium contents up to 12% is due, at least in part, to the relatively high test temperatures used. These temperatures were selected to assure that scale would form at a rate that was compatible with a reasonable test time. Running the ACES burner at lower temperatures for extended periods of time was not technically or economically feasible. Generally, the test temperatures used were above the recommended service temperatures for the alloys tested. The erodent particle sizes and test velocities were representative of those which occur in coal gasification processes.

The dominance of the corrosion process at all conditions of temperature, alloy composition, particle size and other erosion conditions was unexpected. It was thought that when at least the 100μm Al_2O_3 particles were used, the erosion process would be able to sweep oxide off the surface as it formed. The mechanism of elevated temperature corrosion when the oxidizing surface is being mechanically affected during the process by impacting particles must follow different rate laws than those that have been determined to be applicable to static corrosion. Parabolic and linear rates of corrosion are probably replaced by accelerating rates of some type which are not defineable at this time.

One of the problems that is associated with determining the kinetics of the corrosion process is the inability to precisely measure

the metal surface regression rate. The best kinetic work in straight corrosion is carried out using weight change measurements. In the present case where different reactions occur on the front and back surfaces of the same specimen weight change measurements are not appropriate. Efforts are underway to develop an alternative method to measure the rates in a precise enough manner to use for kinetic analysis. The most promising method tested so far involves bonding of a thin strip of platinum on the surface with a Sauereisen cement to protect a portion of the exposed surface. After the test, a cross section of the surface through the protected area shows a difference in metal thickness between the protected and unprotected areas.

A pattern developed in the test series using 5μm coal ash particles that somewhat related the scale morphology to the test temperature, chromium content of the alloy, and whether near static corrosion or combined erosion-corrosion was occurring. Its meaning, if indeed there is one, is not known. As the chromium content, the test temperature, and the severity of the surface environment (corrosion compared to erosion-corrosion) increased, the dominant shape of the iron oxide particles on the surface progressed from nodules to needles to columns. A less than thorough review of the literature failed to shed light on why this pattern occurred.

Erosion-Corrosion Mechanism

The occurrence of Fe_2O_3, free of chromium, as the outer scale of a duplex or multi-layer scale structure with iron-chromium oxide spinel beneath the α-Fe_2O_3 relates to several factors. Among them are the

partial pressure of oxygen at the scale-gas interface compared to that nearer the scale-metal interface, the short growth time of the scales, the difference in the outward diffusion rates of iron and chromium and their diffusion paths. Its occurrence on the higher chromium steels in this study as well as on the low chromium steels differs from the work reported in Reference 8. However, the meticulous observations by Mitchell and his co-workers of the nucleation and growth of oxides on chromium containing steels in the temperature range 400°-950°C in Reference 7, 8 and in their other work promises to be a valuable aid in the effort that is being carried out to gain an understanding of how and why the scales reported on herein occurred in the manners that were observed.

The formation of needles, columns and rosettes or nodules of iron oxide on the surface is due to the manner in which iron diffuses upward and outward from oxide nuclei which form early in the oxidation process. It has been observed that the formations of needles are single crystals of α-Fe_2O_3 as reported in Reference 6. They grow from the tip upward as the result of fast diffusion paths along both their outside surfaces, and along the inner surface of tunnel walls that extend up the columns toward the tip. These surface short circuit diffusion paths are reported to be up to 9 times faster for iron than iron bulk diffusion in the α-Fe_2O_3 and 4 times faster than grain boundary diffusion.[6]

In Reference 7 Mitchell and co-workers describe the manner in which the oxides nucleate and grow in low (3%) and high (18%) chromium steels. He has postulated that the nuclei of the growth oxide crystals

precipitate between a thin oxide film of uniform thickness that pre-exists on the metal surface itself. For low chromium content alloys, the nuclei grow upward and outward to become the iron oxide needles or columns observed herein. Rosettes are also formed such as those seen in Figure 21. Similar rosettes are shown in Reference 8. For higher chromium content alloys, 9, 12, 18% Cr were reported, the nuclei are iron-chromium spinels and they grow inward.

The proposed mechanism of growth for the iron oxide is diagramed in Reference 7. It entails surface diffusion of iron along the pre-existing oxide film to the nuclei sites. Once the nuclei have reached a critical size, no more nuclei are precipitated and the ones that are present grow laterally as well as upward until they impinge on adjacent ones. The keys to the formation of the nuclei which become the needles and columns of oxide appear to be the fast diffusion path of iron atoms along the interface of the pre-existing oxide and the protected location for nucleation between the pre-existing oxide film and the base metal.

Translating the mechanism in Reference 7 to this study, on the corrosion side the pre-existing film remains relatively intact and the iron can rapidly diffuse along it to many protected nuclei growth locations between the film and the base metal. Hence the columns formed are relatively small in diameter and many in number. On the erosion-corrosion side, the pre-existing oxide film is broken up by the early impacting erodent particles, permitting nucleation of oxide precipitates at relatively few sites where the oxide film was not struck and is still intact. These fewer nuclei can then grow to much

larger diameter columns before they impinge on adjacent crystals. This mechanism could be the basis for the large differences between the size of the columns on the corroded side and on the eroded-corroded side of the test specimens.

For higher chromium content alloys, Mitchell included 9, 12 and 18% Cr steels in Reference 7, inward growing iron-chromium oxide spinels are nucleated by the mechanism discussed above. While the study reported on herein found that the outer scale layer was always iron oxide, inner scales of iron-chromium oxide spinels were observed. These spinels, as reported in Reference 7 and 8 could be either (Fe,Cr) $(Fe,Cr)_3O_4$ or α-$(Fe,Cr)_2O_3$. The light and dark areas shown in the inner, spinel scale layer for the 410SS in Figure 21 could be evidence that both spinels were present.

Scale Morphology, Thickness, Composition Differences

The significant increase in the thickness of the scale on the erosion-corrosion side of the test specimens compared to the corroded only side and the change in the distribution of the iron oxide and the spinel thicknesses between the corroded and eroded-corroded sides cannot be explained yet. They were a consistently occurring phenomina for all of the alloys tested with the degree depending on the composition of the alloy and the size of the eroding particles. The effects increased with increasing erodent particle size. Figure 12 shows a comparatively minor difference for 410SS when 5μm flyash was the erodent while Figure 19 shows a major difference when 100μm Al_2O_3 particles were used. An intermediate difference in the thickness is shown for the 2 1/4Cr1Mo steel in Figure 18. Also, the scales on the

eroded-corroded side were thicker when 100μm erodent particles were used than when smaller particles were used. Compare Figures 21 and 22 for the 9Cr and 12Cr steels.

Dynamic corrosion tests were run on all of the test alloys and the results on 410SS, which are typical, are shown in Figure 20. The difference in scale thickness between the corroded and eroded-corroded sides of the same specimen was determined to not be due to dynamic corrosion effects. The ability of the impacting erodent particles to increase the growth rate of the oxide scale without removing it was demonstrated.

In the presence of chromium, the formation of $Fe_{(1-x)}O$ at the metal interface is suppressed and, instead Fe_3O_4 forms.[7] In Figure 19, beneath the iron-chromium spinel scale and next to the base metal, another layer of scale can be seen that does not contain any chromium and, hence, is probably Fe_3O_4. The Fe_3O_4 that forms in the nuclei that grow into needles or columns is transformed to α-Fe_2O_3 sometime during the growth process.[7, 8]

The description of the formation of a multi-layer scale on Fe-3% Cr steel by Mitchell in Reference 8 matches perfectly with the scale on 2 1/4Cr1Mo steel on the corroded side shown in Figure 18. He described an inner, thin layer of $(Fe,Cr)_3O_4$ spinel, a thicker, compact middle layer of Fe_3O_4 and a thin outer layer of α-Fe_2O_3. Since positive identification of each scale layer was made by Mitchell and he identified a distinct layer of Fe_3O_4, it is assumed that layers of Fe_3O_4 are present on some of the other lower chromium content steels, in addition to the scale shown in Figure 18, that are reported on

herein. To date, only SEM X-ray maps of the principal elements present have been used in this study to aid in the identification of scales.

In Reference 8 Mitchell reported the occurrence of considerable porosity in the oxide scales. He observed that more and smaller diameter pores occurred in the higher chromium content alloys. The same observation was made in this study, but primarily in the scale on the erosion-corrosion side of the specimens. Compare Figure 19 of 410SS with Figure 18 of 2 1/4Cr1Mo steel.

The effect of the test temperature on the surface morphology of the scales on the erosion-corrosion sides of the specimens was very pronounced when 5μm and 100μm particles were used as the erodent, Figures 25 and 23, but caused very little change when 50μm particles were used, Figure 24. The reason for this apparent anomaly is not known.

CONCLUSIONS

1. Corrosion is the dominant mechanism at all test conditions in the erosion-corrosion of chromium containing steels at temperatures from 700°-1000°C.

2. The erosion process enhances the growth of oxide scales.

3. The erosion process markedly changes the morphology and composition distribution of the oxide scales.

4. The morphology of the surface oxides are changed as the erodent particle size and test temperatures are changed.

5. As the test temperature and the chromium content of the alloys increased, the dominant shape of the iron oxide particles on the surface of the scale progressed from nodules to needles to columns. The reason for this and its meaning are not known.

6. Iron oxide (α-Fe_2O_3) forms as the outer scale in a multi-layer scale on all of the chromium containing steels tested. The inner scale layers consist of iron-chromium oxide spinels and Fe_3O_4, depending on the chromium content of the alloy.

7. Dynamic corrosion is not a contributor to the increase in the scale thickness on the erosion-corrosion sides of the test specimens, compared to the corrosion side.

8. Larger erodent particles result in thicker scales.

9. The eroded scale surface became smoother as the erodent particle size increased.

10. Additional studies must be performed to gain a clearer understanding of the mechanisms involved.

ACKNOWLEDGEMENT

Research sponsored by the U.S. Department of Energy under DOE/FEAA 15 10 10 0, Advanced Research and Technical Development, Fossil Energy Materials Program, Work Breakdown Structure Element LBL-3.5 and under Contract No. DE-AC03-76SF00098.

REFERENCES

1. Natesan, K., "Corrosion Behavior of Materials in Low and Medium BTU Coal Gasification Environments", Proceedings, NACE Conference on Corrosion-Erosion-Wear of Materials in Emerging Fossil Energy Systems, pp 100-126, Berkeley, CA, January, 1982.

2. Perkins, R.A., Morse, G., and Coors, W.C., "Materials for Syngas Coolers", EPRI AP-2518, Final Report, August, 1982, EPRI, 3412 Hillview Avenue, Palo Alto, CA 94304.

3. Whittle, D.P. and Hindam, H., "Microstructure and Growth of Protective Cr_2O_3 and Al_2O_3 Scales at High Temperature", Proceedings, NACE Conference on Corrosion-Erosion-Wear of Materials in Emerging Fossil Energy Systems, pp 54-99, Berkeley, CA, January, 1982.

4. Birks, N. and Meier, G., "Mechanism of Corrosion in Multiple Component Gases at High Temperatures", Proceedings, NACE Conference on Corrosion-Erosion-Wear of Materials in Emerging Fossil Energy Systems, pp 1-53, Berkeley, CA, January 1982.

5. Hill, V.L. and Humphreys, B.A., "Mechanism of Corrosion of Structural Alloys in Coal Conversion Atmospheres", Proceedings, ASM Conference on The Properties and Performance of Materials in the Coal Gasification Environment, pp 257-288, Pittsburgh, PA,

6. Voss, D.A., Butler, E.P. and Mitchell, T.E., "The Growth of Hematite Blades During the High Temperature Oxidation of Iron", Met. Trans. A, V. 13A, pp 929-935, May, 1982.

7. Kuroda, K., Labun, P.A., Welsch, G., and Mitchell, T.E., "Oxide-Formation Characteristics in the Early Stages of Oxidation of Fe and Fe-Cr Alloys", Oxidation of Metals, v. 19 no. 3/4, pp 117-127, 1983.

8. Kuroda, K., Labun, P.A., Welsch, G., and Mitchell, T.E., "Microstructural Studies of the Oxidation of Fe-Cr Alloys", Proceedings JIMIS-3, High Temperature Corrosion Transactions of the Japan Institute of Metals, Supplement, 1983.

9. Foerster, T.F.W., Levy, A.V. and Newman, J.S., "Corrosion of Metals in Coal Char Environments", NACE International Corrosion Conference Series no. 6, pp 354-362, San Diego, CA, March, 1981.

10. Douglass, D.L., Bhide, V.S., and Vineberg, E., "The Corrosion of Some Superalloys in Contact with Coal Chars in Coal Gasifier Atmospheres", Oxidation of Metals, v. 16, nos. 1/2, pp 29-80, August, 1981.

11. Silence, W.L., Hill, V.L., and Vesely, E.J., "The Effects of Environmental Variables on the Erosion-Corrosion Behavior of Candidate Materials for Coal Conversion Plants", Proceedings ASM Conference on The Properties and Performance of Materials in the Coal Gasification Environment, pp 629-694, Pittsburgh, PA, September, 1980.

12. Levy, A., "The Erosion of Metal Alloys and Their Scales", Proceedings NACE Conference on Corrosion-Erosion-Wear of Materials in Emerging Fossil Energy Systems, pp 298-376, Berkeley, CA, January, 1982.

13. Quadir, T. and Shewmon, P., "Solid Particle Erosion Mechanisms in Copper and Two Copper Alloys", Met. Trans. A, V. 12A, pp 1163-1176.

14. Emiliani, M. and Brown, R., "Erosion of Ti 6Al-4V by Spherical Silica Particles at 90° Impact Angle", Proceedings of 6th International Conference on Erosion by Liquid and Solid Impact", pp 48-1, Cambridge University, Cambridge, England, September, 1983.

15. Cousens, A.K. and Hutchings, I.M., "A Critical Study of the Erosion of an Aluminum Alloy by Solid Spherical Particles at Normal Impingement", Proceedings of ASME Conference on Wear of Materials 1983, pp 382-389, Reston, VA, April, 1983.

16. Zambelli, G. and Levy, A.V., "Particulate Erosion of NiO Scales", WEAR v. 68 no. 3, pp 269-288, May, 1981.

17. Maasberg, J.A. and Levy, A.V., "Erosion of Elevated Temperature Corrosion Scale on Metals", WEAR v. 73, no. 2., pp 355-370, November, 1981.

18. Schaefer, A.O. and Veseley, E. Jr., "MPC 4.4 Erosion-Corrosion of Materials in Coal Gasification Pilot Plants", The Metal Properties Council Subcommittee 9 Report on Materials for Coal Conversion, 1982 Annual Report, Metal Properties Council, Inc., 345 East 47th Street, New York, New York 10017, March, 1983.

19. Nagarajan, V. and Wright, I.G., "Influence of Oxidation Scales on High Temperature Corrosion-Erosion Behavior of Alloys", Proceedings of NACE Conference on High Temperature Corrosion, pp 398-405, San Diego, CA March, 1981.

20. Levy, A.V., and Slamovich, E., "Combined Corrosion-Erosion of Steels in Oxidizing Environments", Paper no. 84, NACE Corrosion 84, New Orleans, LA, April, 1984.

21. Barkalow, R.H., Goebel, J.A. and Pettit, F.S., "Materials Problems in Fluidized Bed Combustion Systems", EPRI Report CS-1448, May, 1980.

22. Wright, I. and Herchenroeder, R., "High Temperature Erosion-Corrosion of Alloys", EPRI Report CS-1454, July, 1980.

FIGURES

1. Two cube shaped specimens in burner duct during testing separated by circular alumina washers. CBB 834-3754

2. Corroded and eroded-corroded surfaces of 1018 steel at 700°C. XBB 833-1825

3. Corroded and eroded-corroded surfaces of 2 1/4Cr1Mo steel at 700°C. XBB 833-1824

4. Corroded and eroded-corroded surfaces of 2 1/4Cr1Mo steel at 800°C. XBB 8210-9326

5. SEM-KEVEX analysis of scale surface on eroded-corroded side of the 2 1/4Cr1Mo steel at 800°C. XBB 837-6076

6. Corroded and eroded-corroded surfaces of 5Cr1/2Mo steel at 800°C and 875°C. XBB 831 590

7. Corroded and eroded-corroded surfaces of 9Cr1Mo steel at 925°C. XBB 820 9329

8. SEM-KEVEX analyses of the oxide column composition of the 9Cr1Mo steel at 950°C. XBB 837 6078

9. Corroded and eroded-corroded surfaces of 9Cr1Mo steel at 800°C and 950°C. XBB 833 1822

10. Corroded and eroded-corroded surfaces of 410SS at 950°C. XBB 820 9325

11. SEM-KEVEX analyses of columns of scale on 410SS at 950°C. XBB 837 6079

12. Cross section of corroded and eroded-corroded surfaces of 410SS at 950°C. XBB 833 1827

13. Corroded and eroded-corroded surfaces of 304SS at 1000°C. XBB 8210 9324

14. Raman spectra of corroded surface of 304SS at 1000°C. XBB 837 10812

15. Raman spectra of eroded-corroded surface of 304SS at 1000°C. XBL 837 10813

16. Effect of eroding particle size on the surface morphology of the eroded-corroded surface of 410SS at 950°C. XBB 837 6248

17. Morphology of surface scale on 5Cr1/2Mo steel eroded by 5μm, 50μm, 100μm particles. XBB 841 100

18. Cross section of scales on 2 1/4Cr1Mo steel from 100μm Al_2O_3 tests at 950°C. XBB 841 98

19. Cross section of scales on 410SS from 100μm Al_2O_3 tests at 850°C. XBB 837 6107

20. Cross section of scales formed on 410SS at 950°C at different test conditions. XBB 841 97

21. Cross section and surface morphology of scales of 2 1/4, 9 and 12Cr steels eroded-corroded at 850°C using 100μm Al_2O_3. XBB 841 96

22. Cross section and surface morphology of scales of 5, 9 and 12Cr steels eroded-corroded at 950°C using 50μm Al_2O_3. XBB 841 105

23. Surface morphology of eroded-corroded 9Cr1Mo steel at three different test temperatures using 100μm Al_2O_3. XBB 841 106

24. Surface morphology of eroded-corroded 9Cr1Mo steel at three different test temperatures using 50μm Al_2O_3. XBB 841 104

25. Surface morphology of eroded-corroded 410SS steel at two test temperatures using 5μm flyash. XBB 841 107

TABLE 1

ALLOY COMPOSITION (NOMINAL)

ALLOY	Cr	Ni	Mo	Si	Mn	C	P/S max	Fe
1018					0.5	0.2	0.09	bal
1 1/4Cr 1Mo	2.2		0.9	0.3	0.4	0.2	0.02	bal
5Cr 1/2Mo	5.1		0.6	0.02	0.5	0.1	0.02	bal
9Cr 1Mo	9		1.0	0.5	0.5	0.15	0.02	bal
410SS	12			1.0	1.0	0.2	0.1	bal
304SS	18	9		1.0	2.0	0.1	0.1	bal

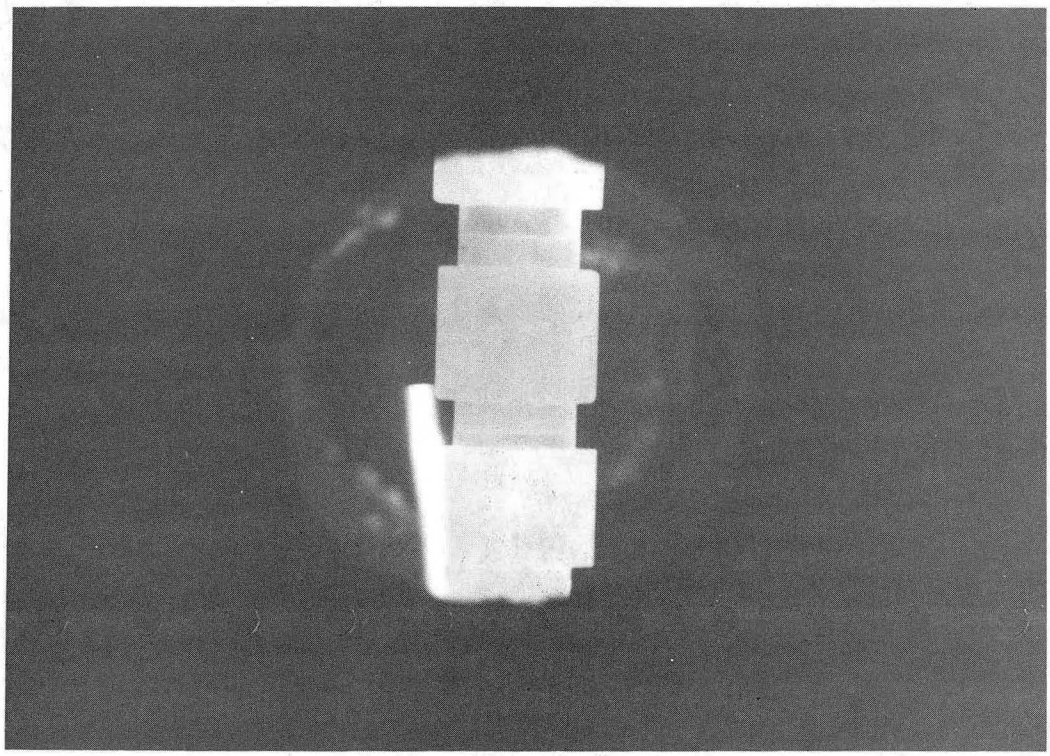

CBB 834-3754

Fig. 1. Two cube shaped specimens in burner duct during testing separated by alumina washers.

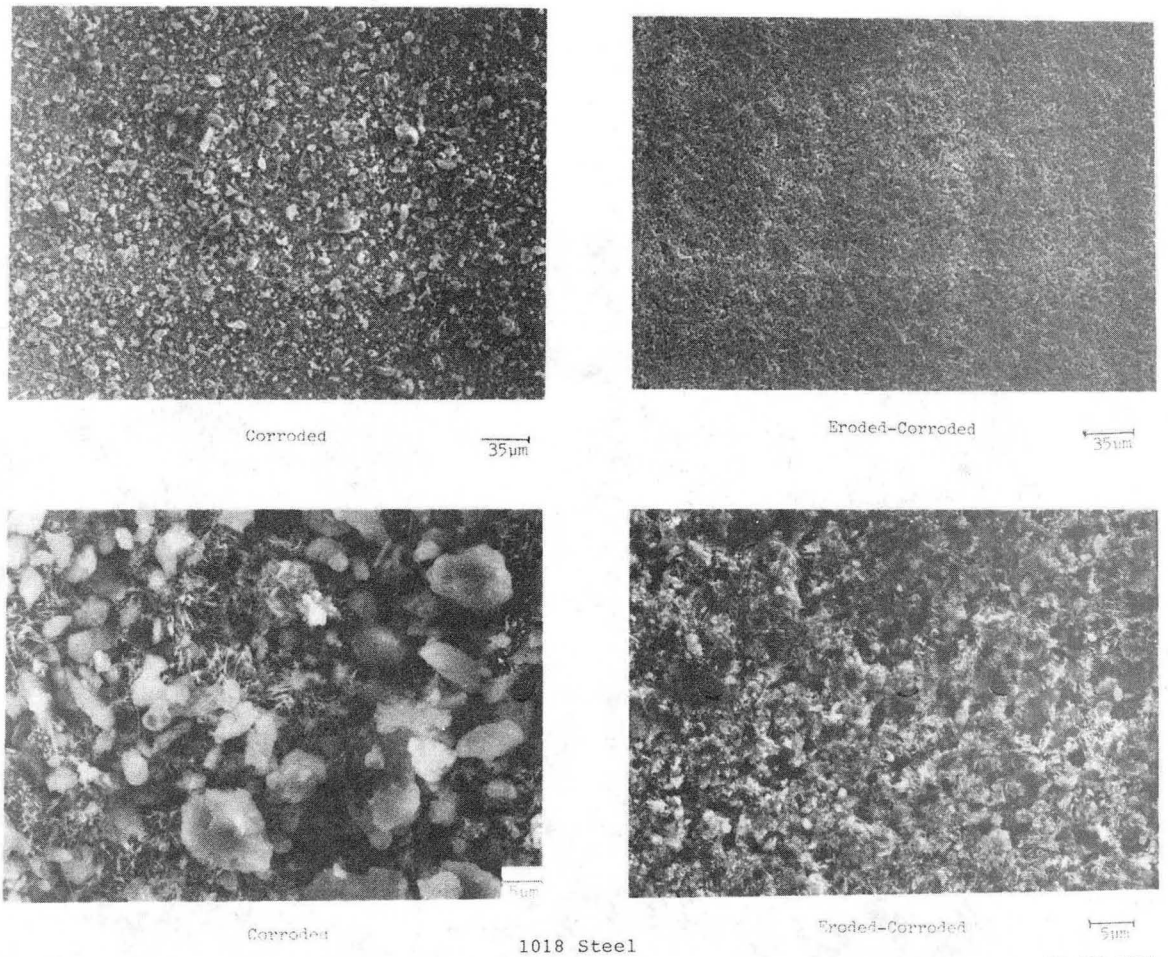

Fig. 2. Corroded and eroded-corroded surfaces of 1018 steel at 700°C

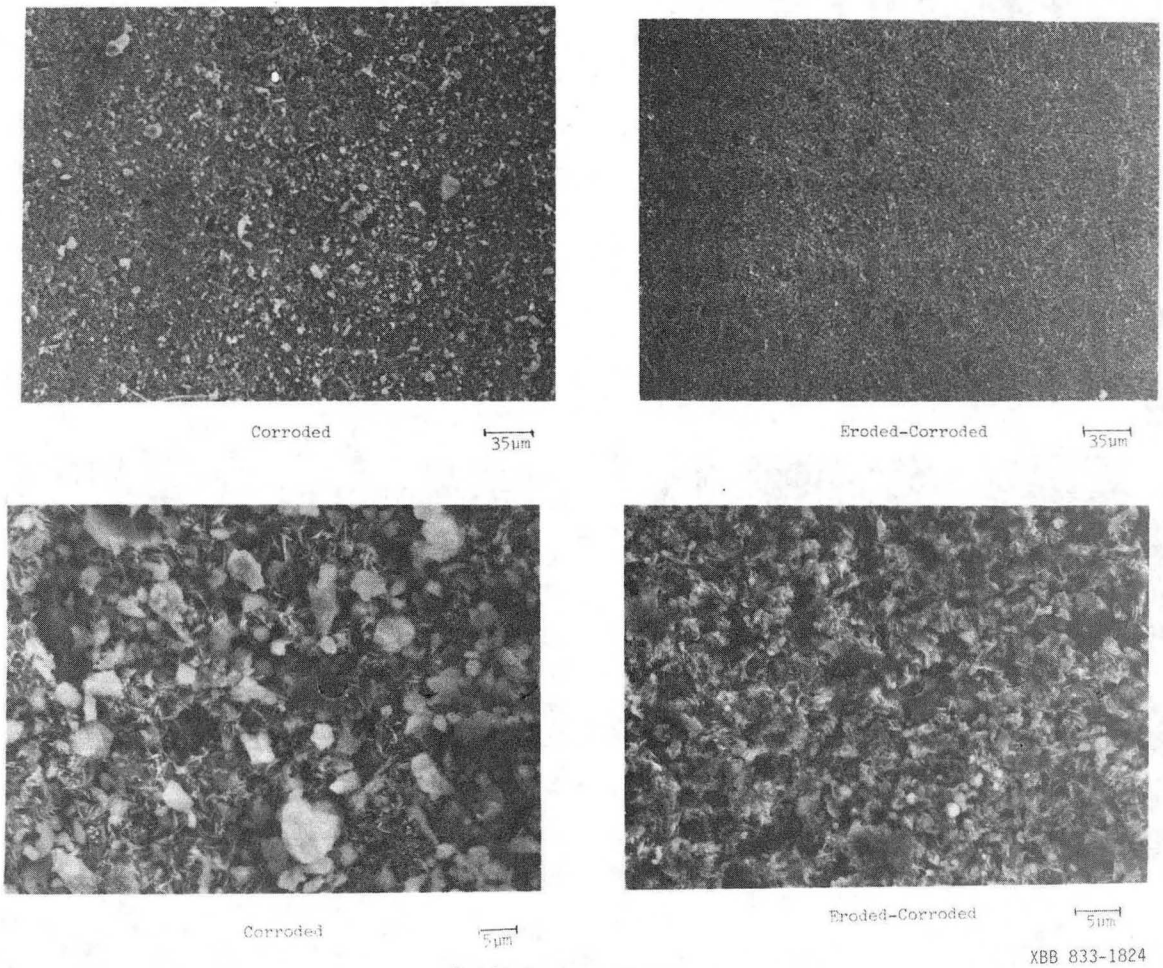

Fig. 3. Corroded and eroded-corroded surfaces of 2 1/4 Cr 1Mo steel at 700°C

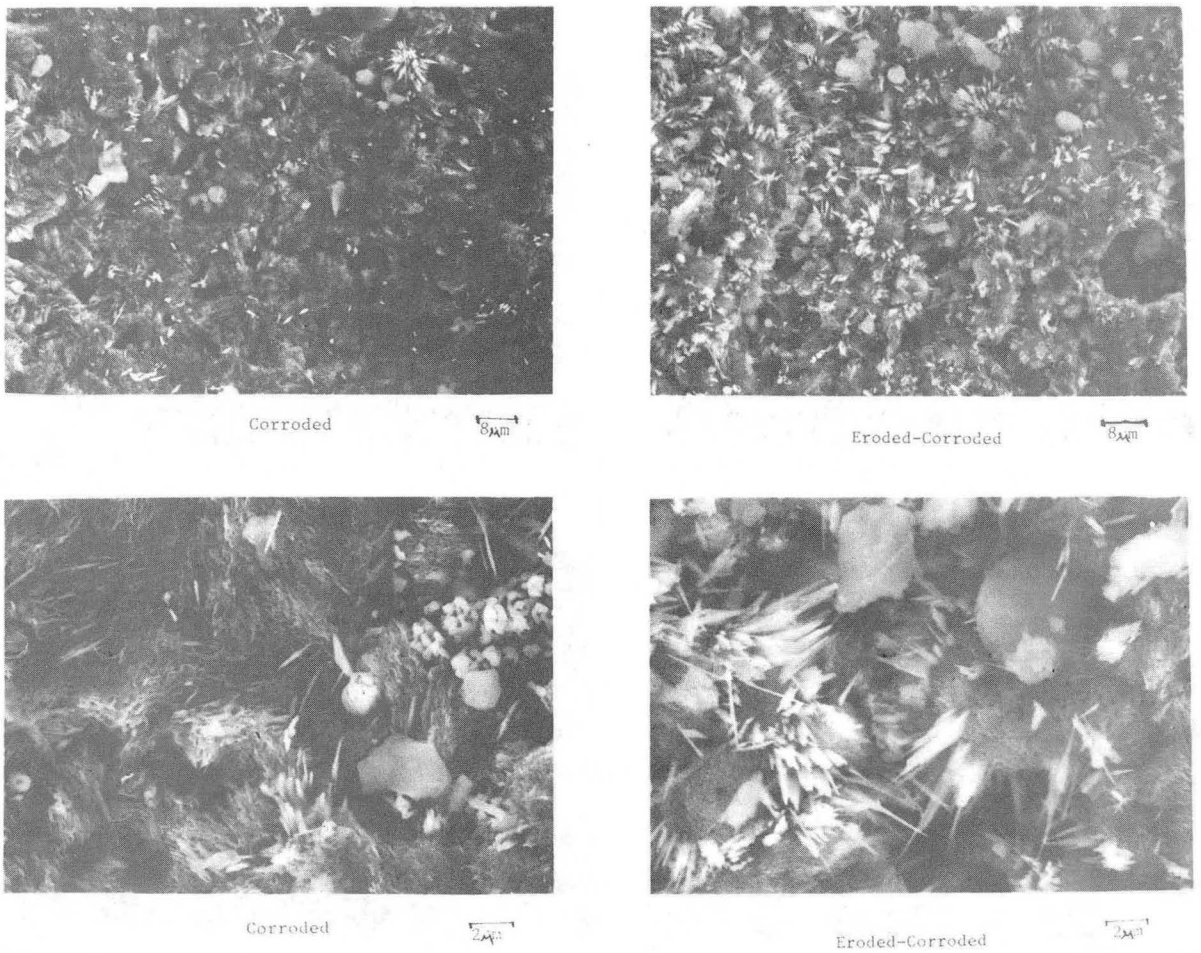

Fig. 4. Corroded and eroded-corroded surfaces of 2 1/4 Cr 1Mo steel at 800°C

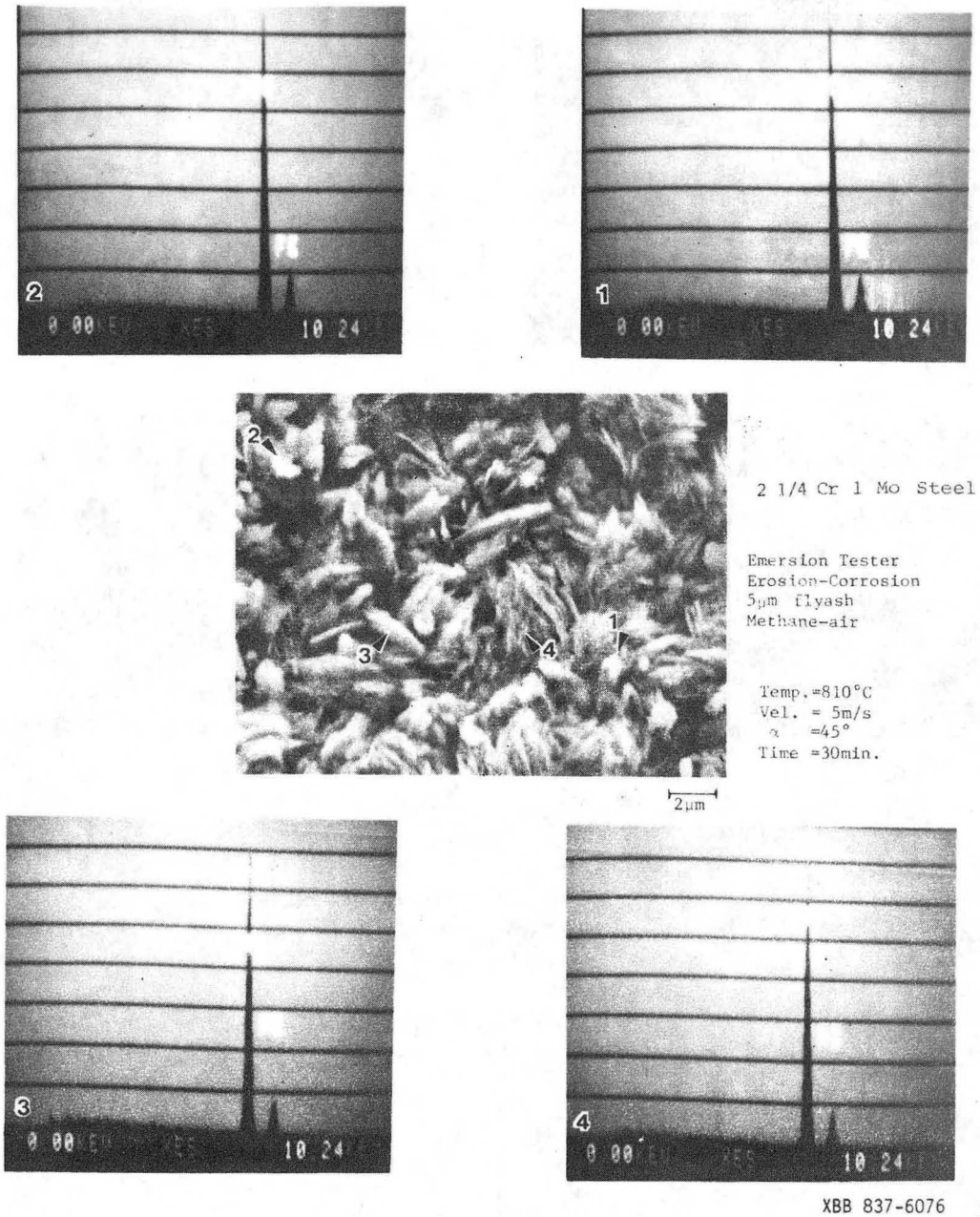

Fig. 5. SEM-KEVEX analysis of scale surface on eroded-corroded side of the 2 1/4 Cr 1Mo steel at 800°C

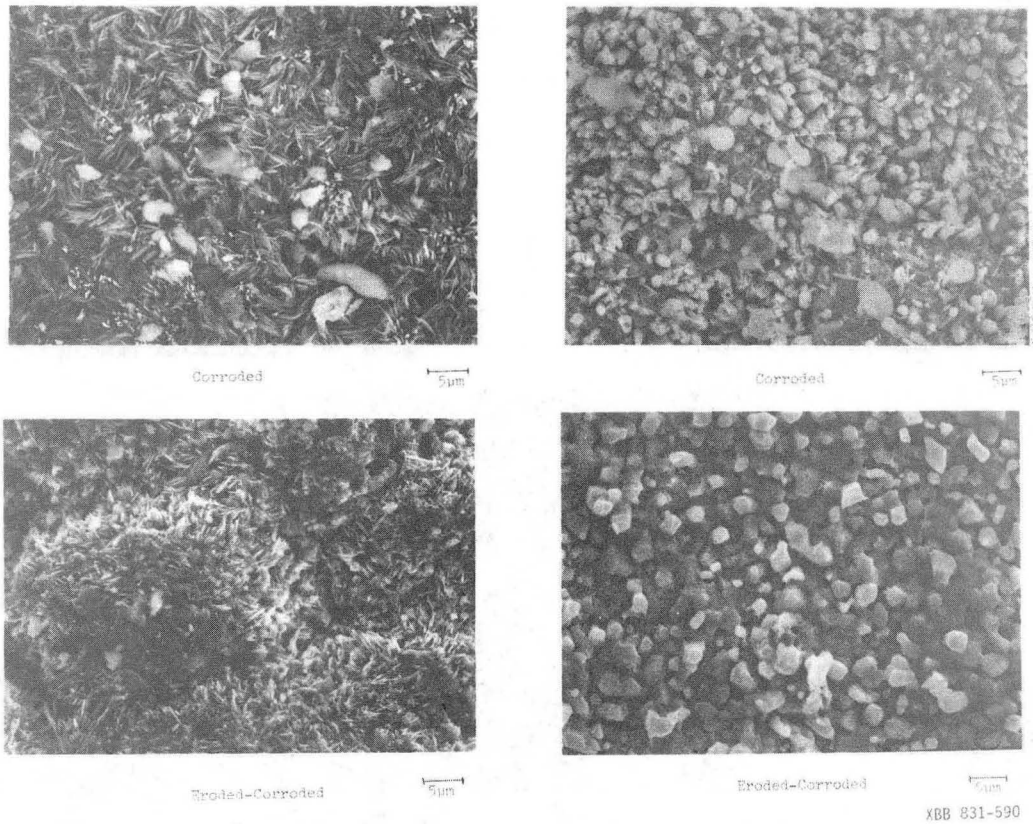

Fig. 6. Corroded and eroded-corroded surfaces of 5 Cr 1/2Mo steel at 800°C and 875°C

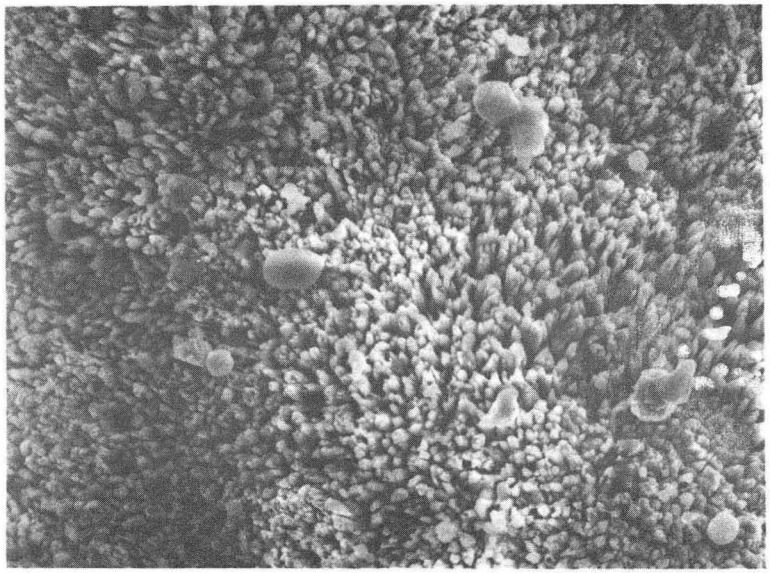

Corroded

10μm

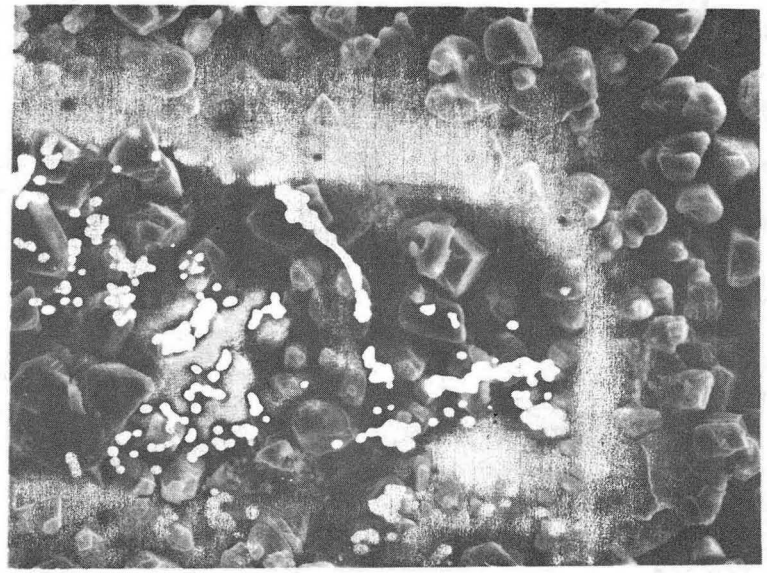

Eroded-Corroded

10μm

9 Cr 1 Mo Steel

Emersion Tester	Temp. =925°C
5μm flyash	Vel. =.5m/s
Methane-air	α =45°
	Time =30min.

Fig. 7. Corroded and eroded-corroded surfaces of 9 Cr 1Mo steel at 925°C XBB 820-9329

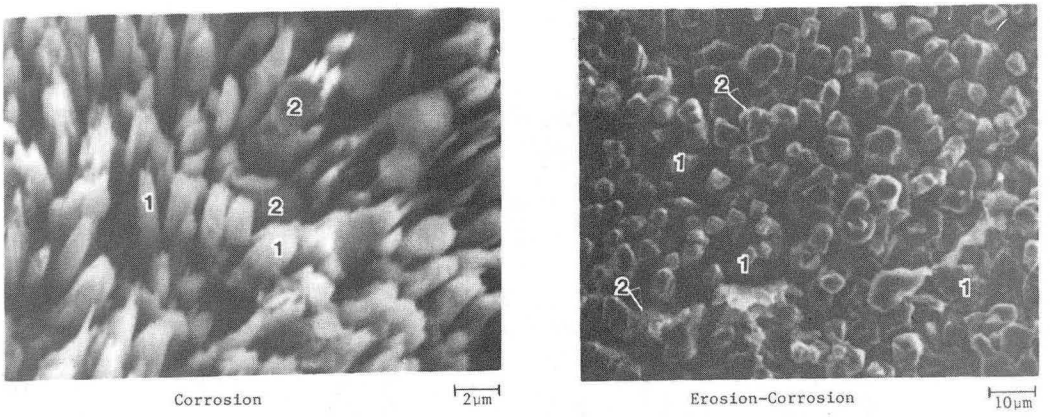

Fig. 8. SEM-KEVEX analyses of the oxide column composition of the 9 Cr 1Mo steel at 950°C

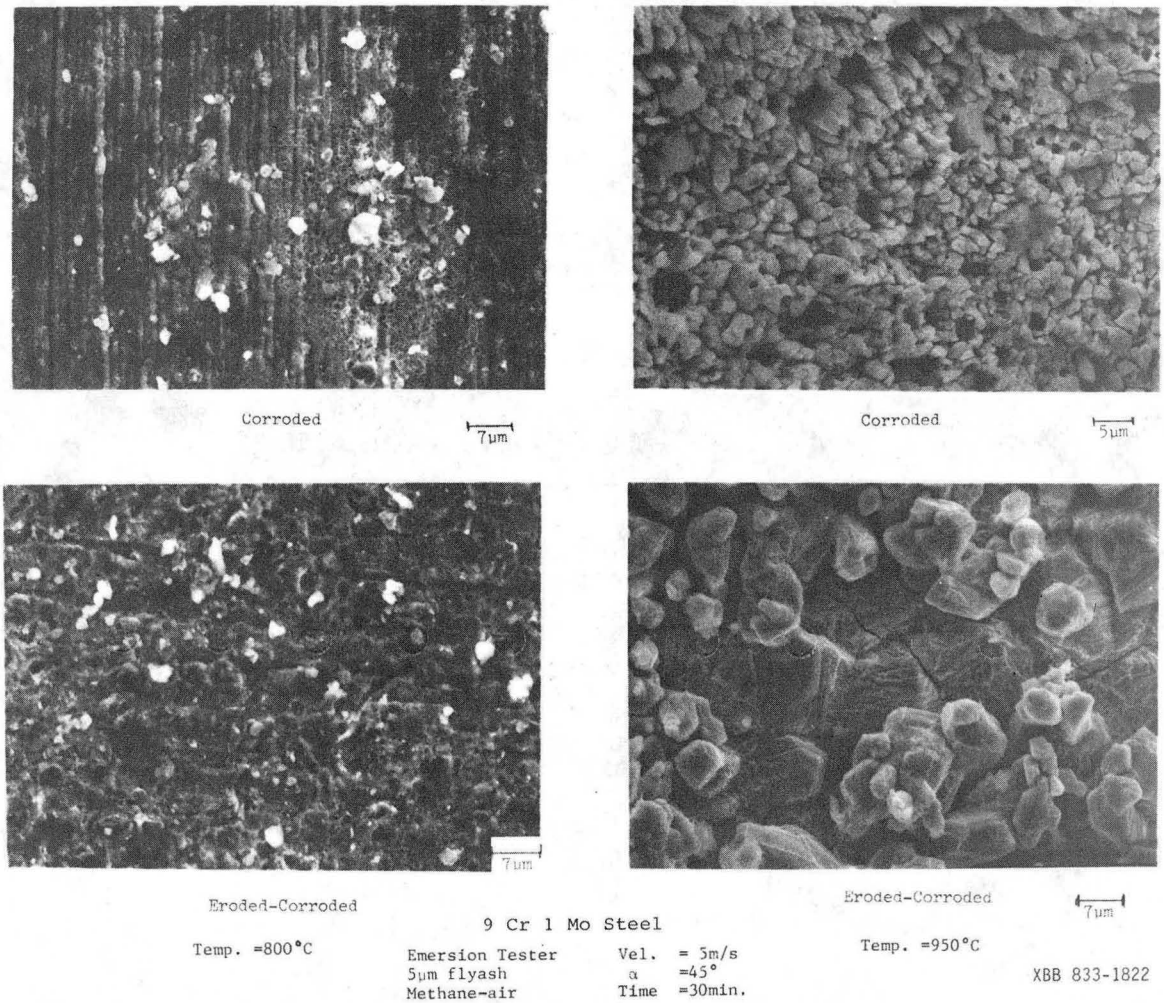

Fig. 9. Corroded and eroded-corroded surfaces of 9 Cr 1Mo steel at 800°C and 950°C

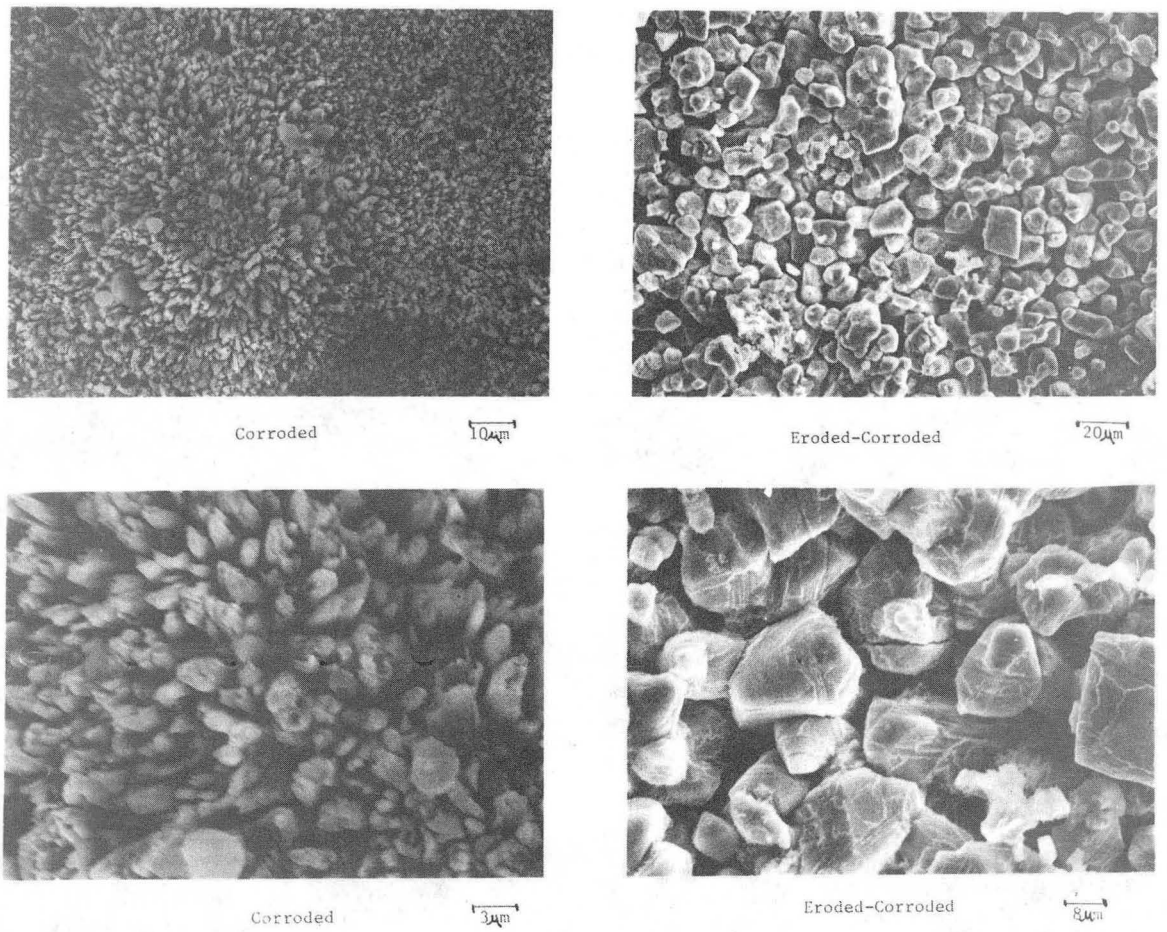

Fig. 10. Corroded and eroded-corroded surfaces of 410SS at 950°C XBB 820-9325

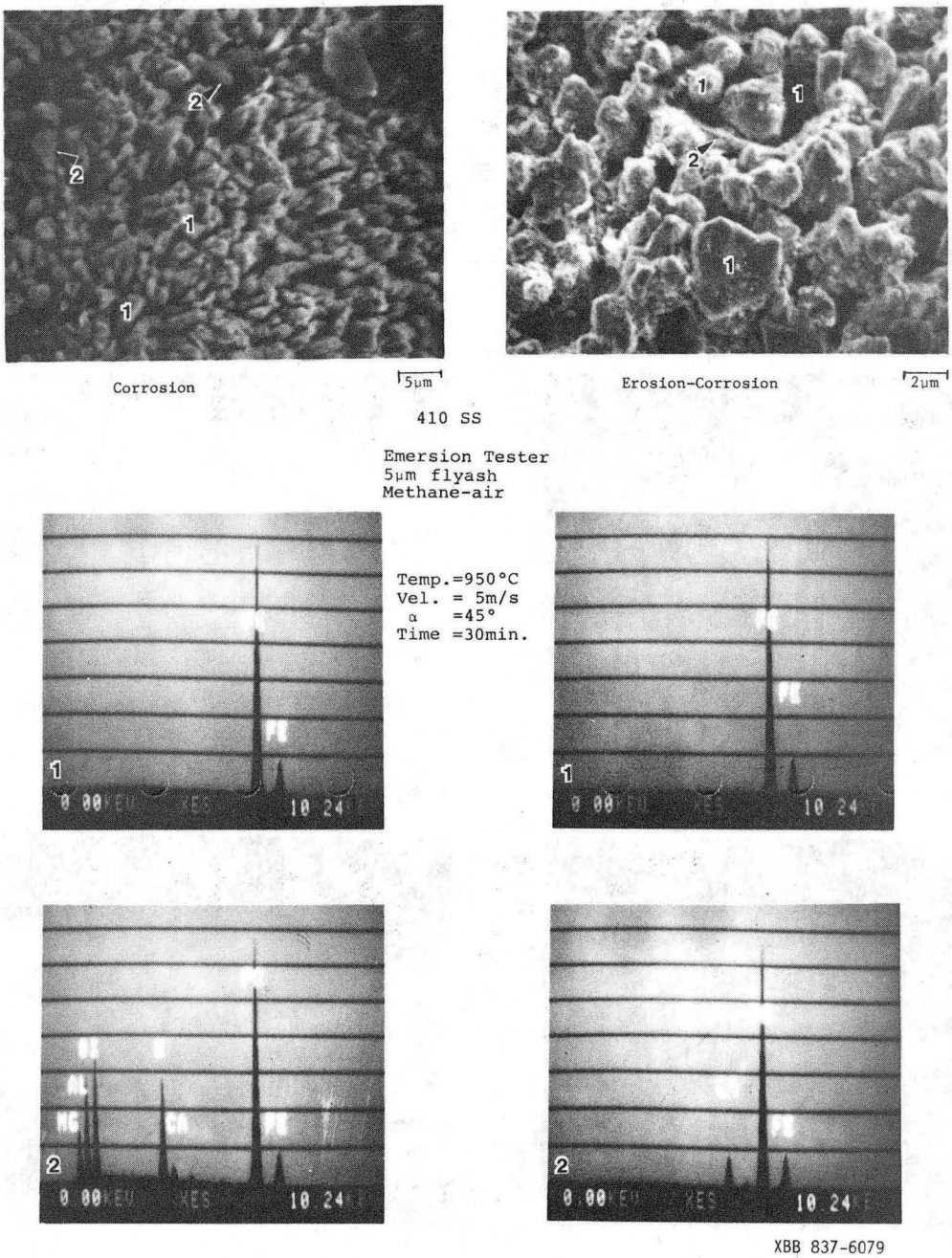

Fig. 11. SEM-KEVEX analyses of columns of scale on 410SS at 950°C

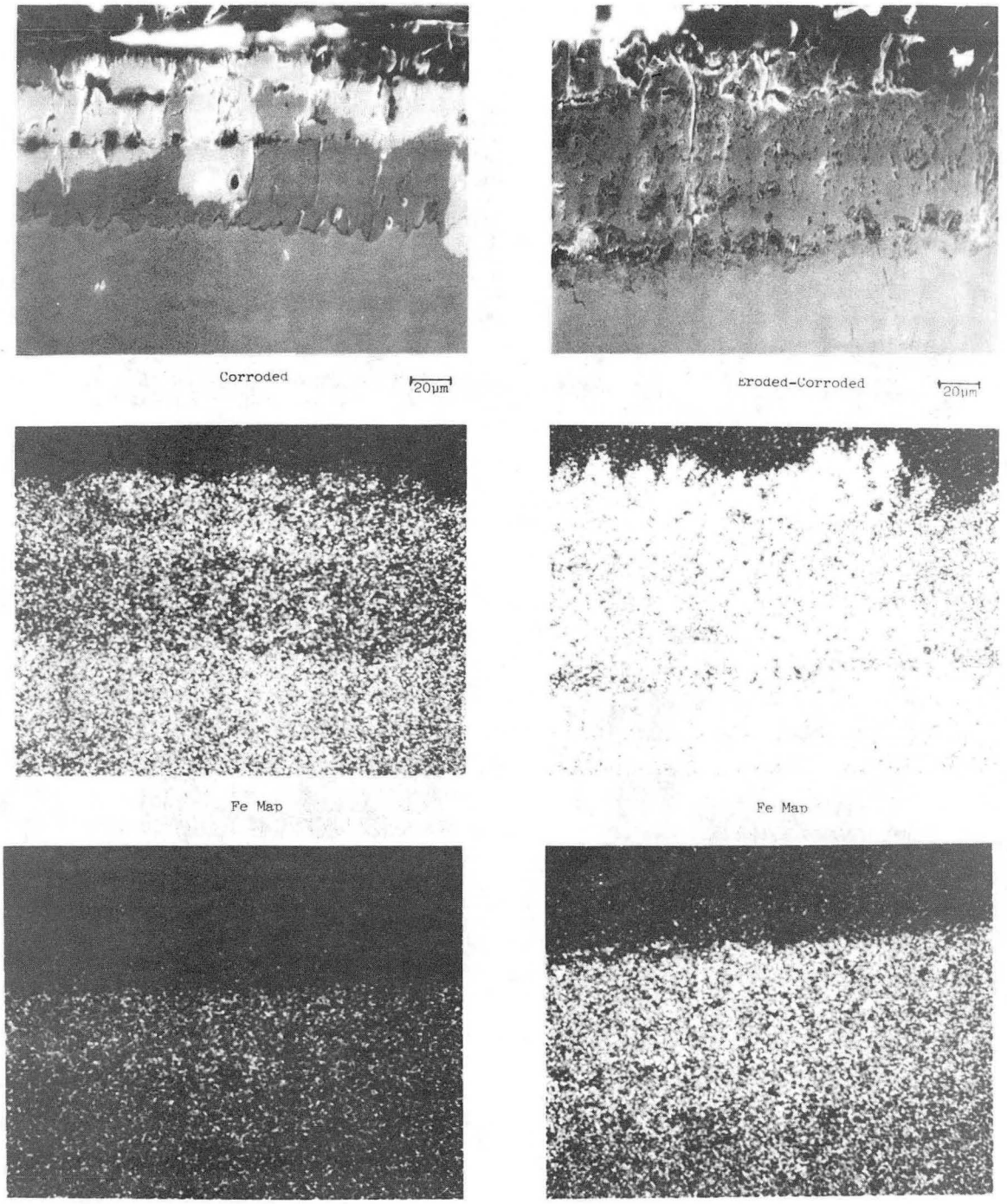

Fig. 12. Cross section of corroded and eroded-corroded surfaces of 410SS at 950°C

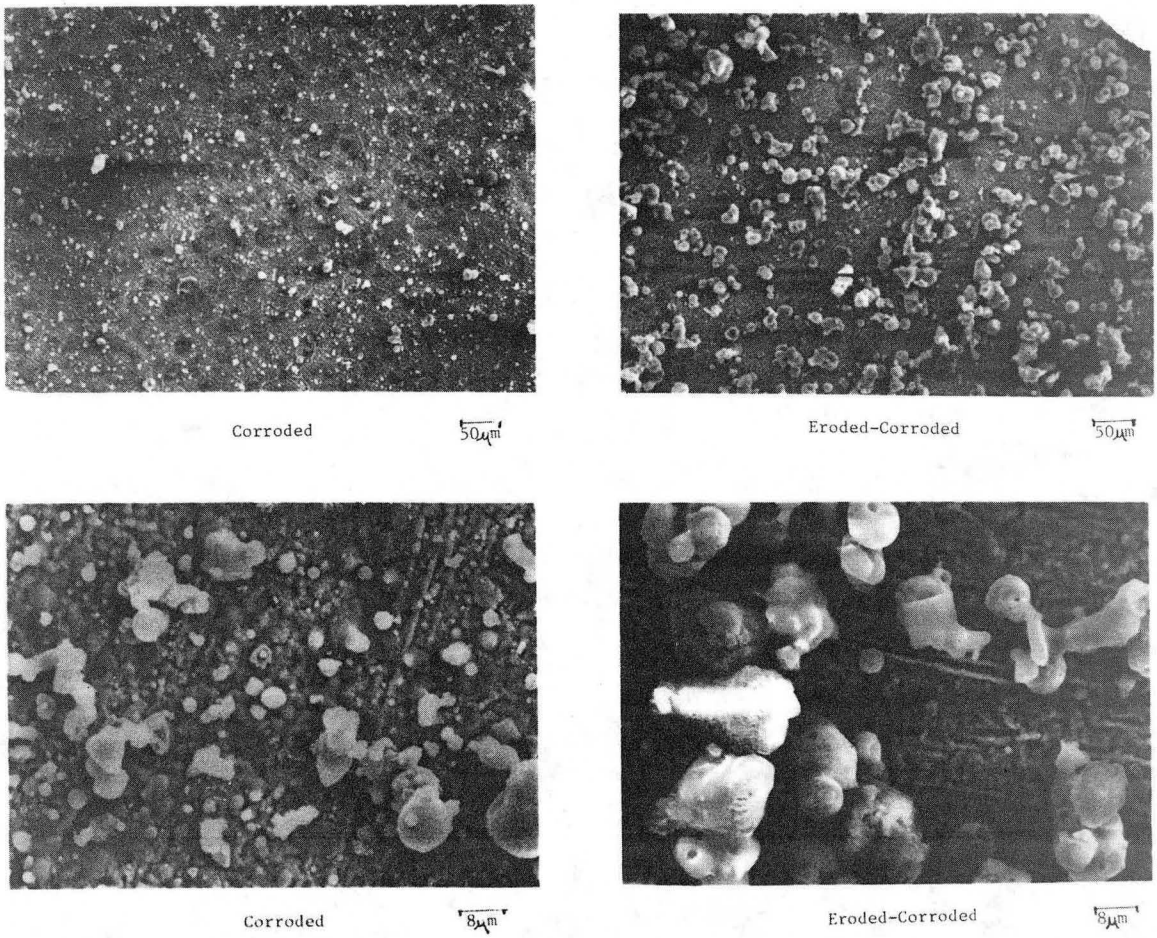

Fig. 13. Corroded and eroded-corroded surfaces of 304SS at 1000°C

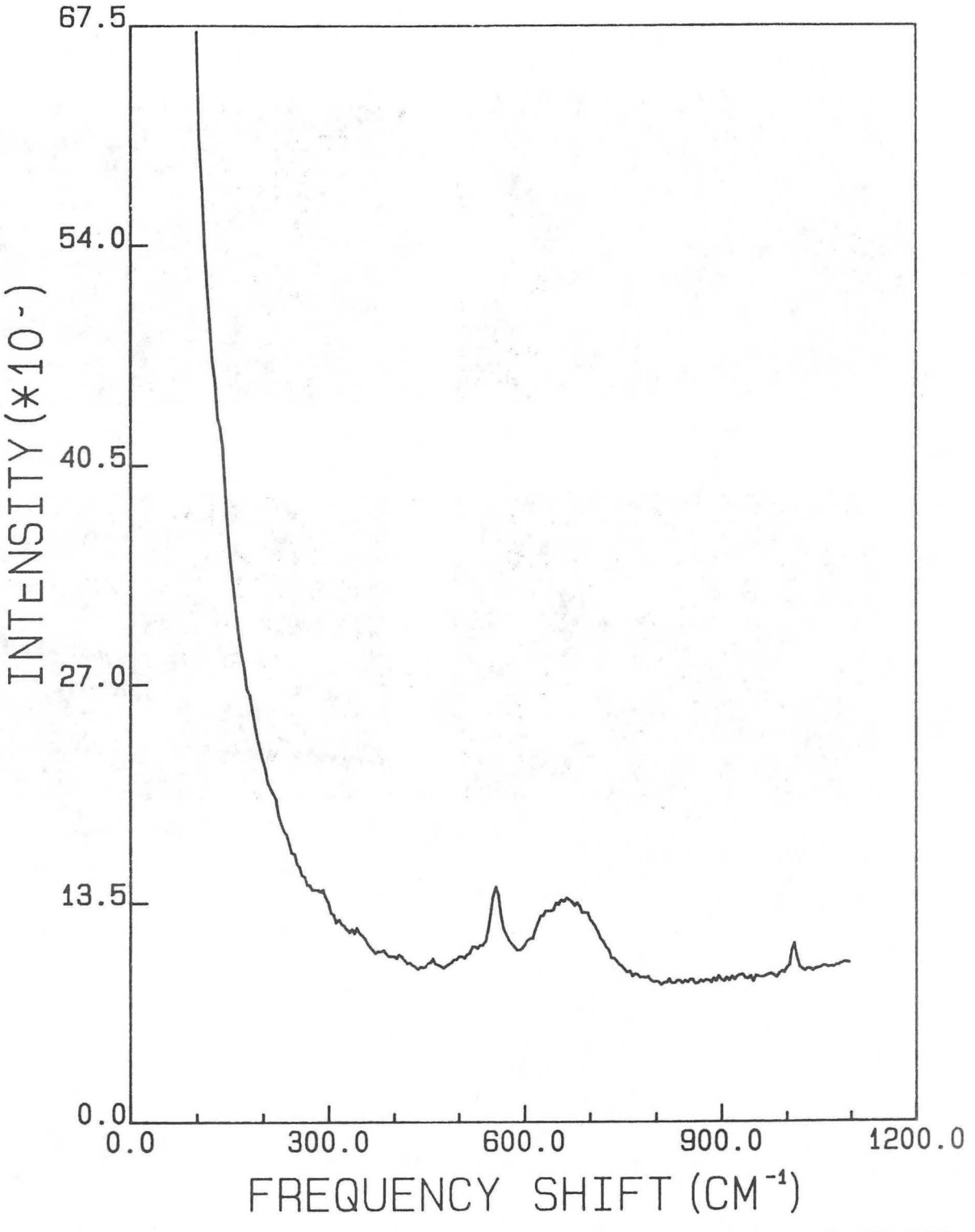

XBL 837-10812

Fig. 14. Raman spectra of corroded surface of 304SS at 1000°C

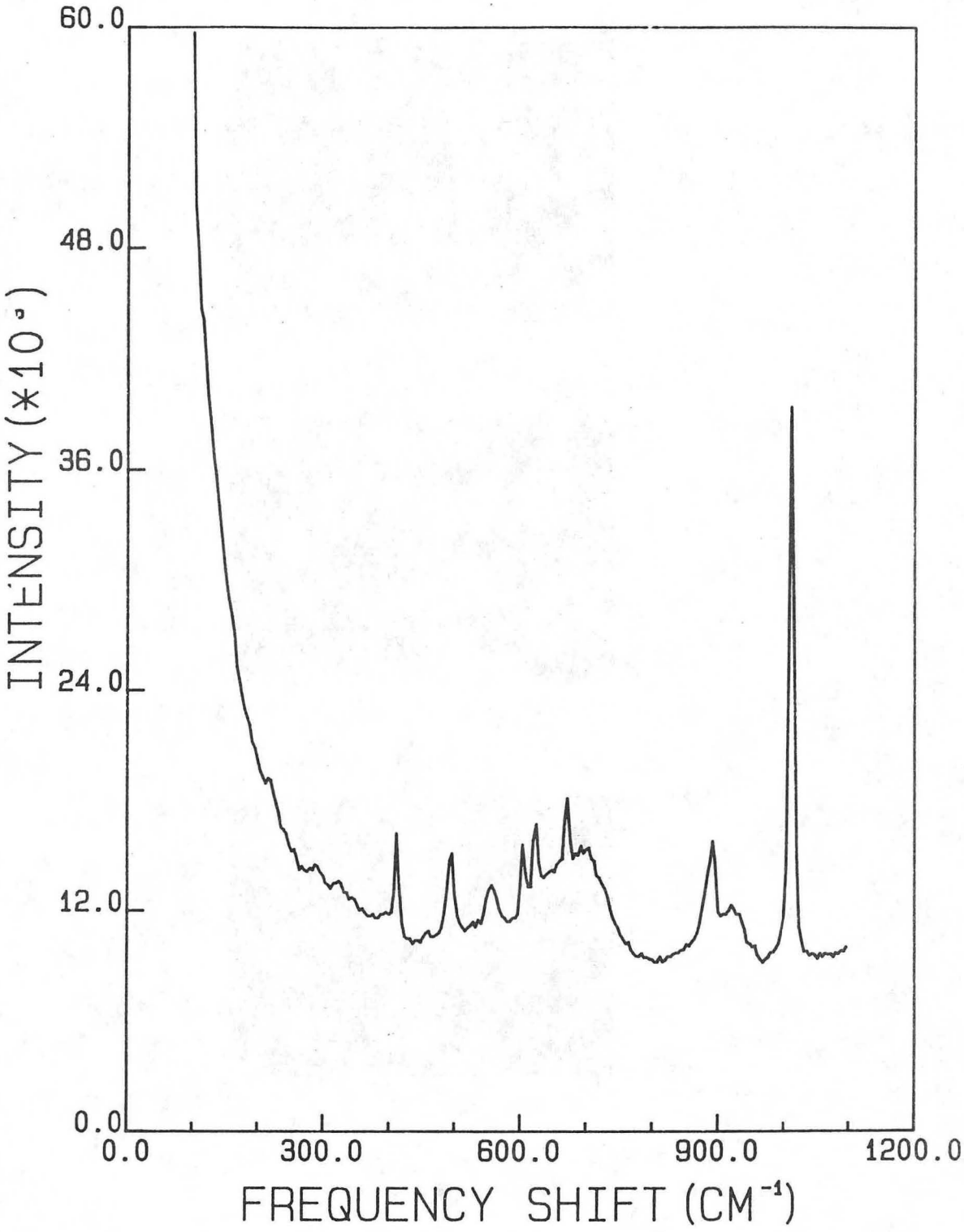

XBL 837-10813

Fig. 15. Raman spectra of eroded-corroded surface of 304SS at 1000°C

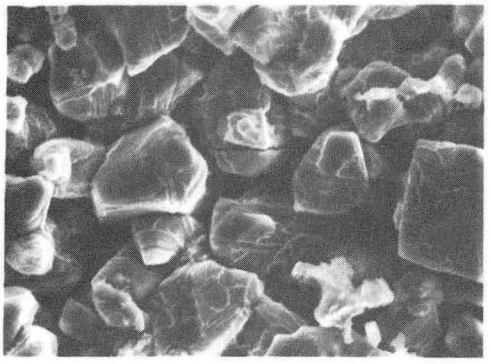

5μm flyash

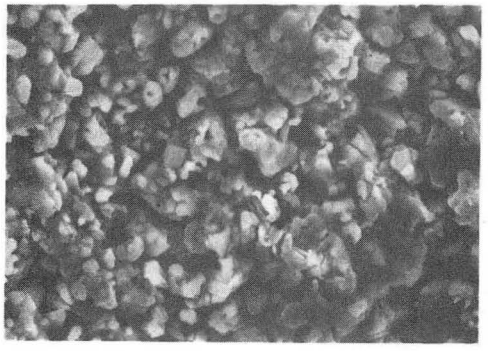

50μm Al_2O_3

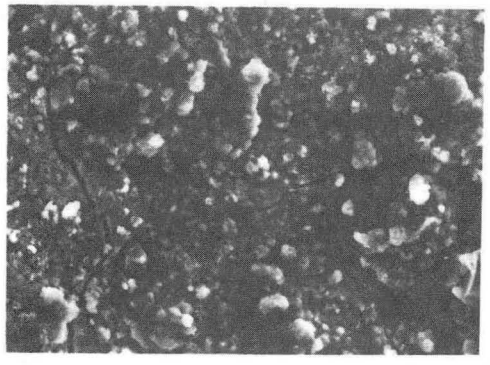

100μm Al_2O_3

410 SS

Emersion Tester	Temp. =950°C
Erosion-Corrosion	Vel. = 5m/s
Methane air	α =45°
	Time =30min.

XBB 837-6248

Fig. 16. Effect of eroding particle size on the surface morphology of the eroded-corroded surface of 410SS at 950°C

5μm flyash

2μm

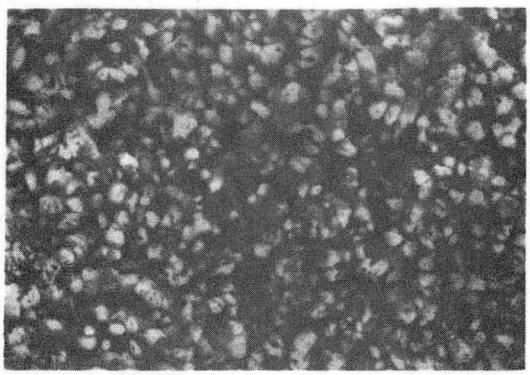

50μm Al_2O_3

3μm

100μm Al_2O_3

10μm

5 Cr 1/2 Mo Steel

Emersion Tester
Erosion-Corrosion
Methane air

Temp. =800°C
Vel. =15m/s
α =45°
Time =30min.

Fig.17. Morphology of surface scale on 5Cr1/2Mo steel eroded by 5μm, 50μm, 100μm particles.

XBB 841-100

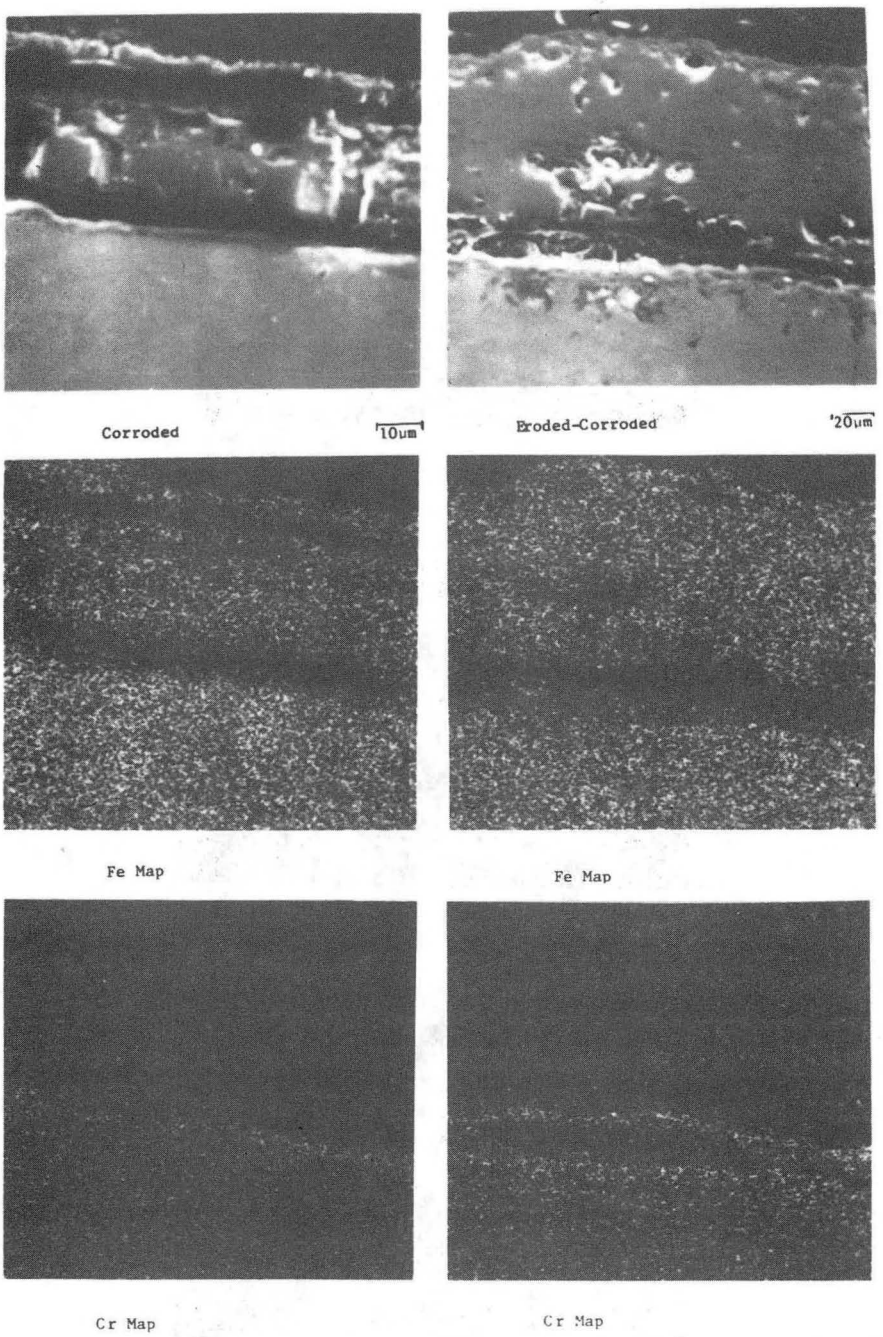

XBB 841-98

Fig. 18. Cross section of scales on 2 1/4 CrlMo steel from 100μm Al_2O_3 tests at 850°C.

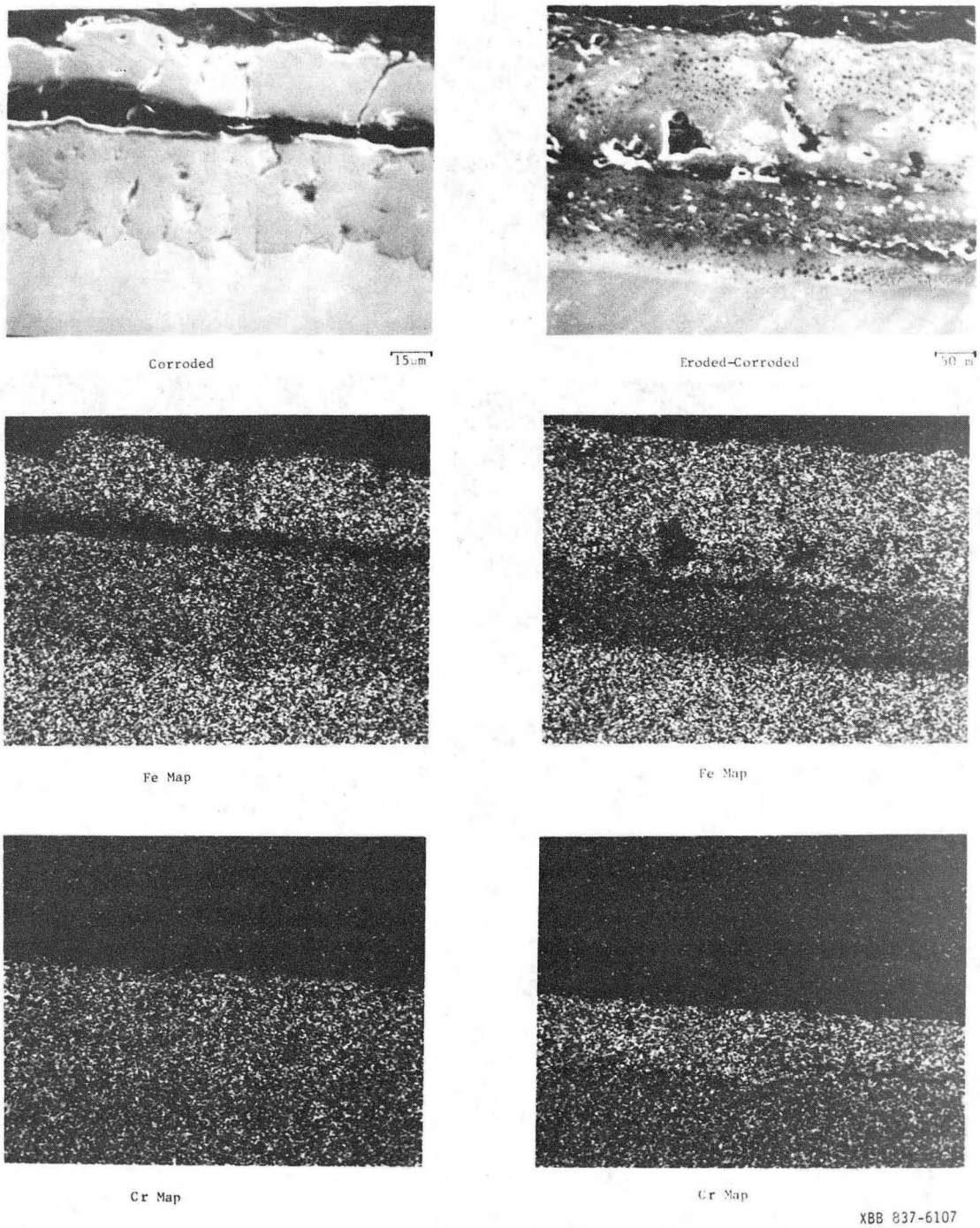

Fig.19. Cross section of scales on 410SS from 100μm Al_2O_3 tests at 950°C.

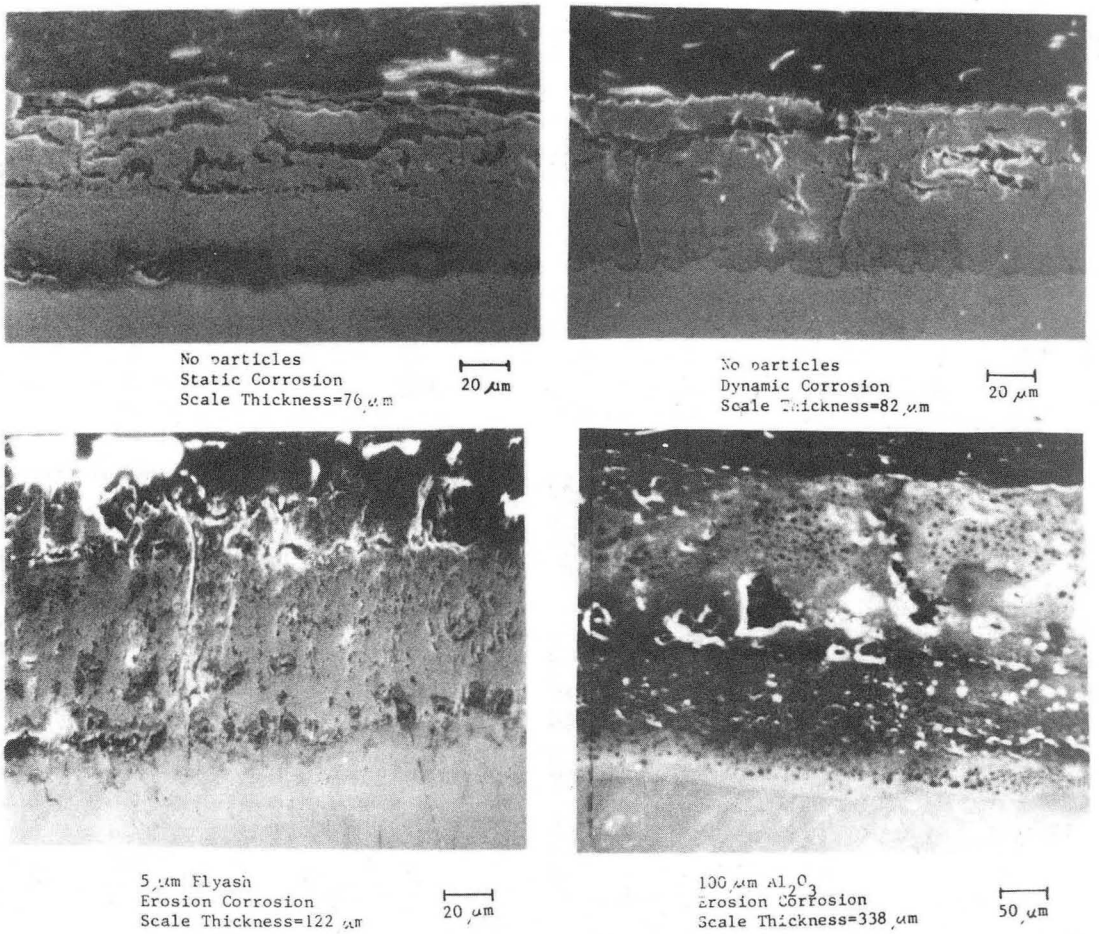

Fig. 20. Cross section of scales formed on 410SS at 950°C at different test conditions.

XBB 841-97

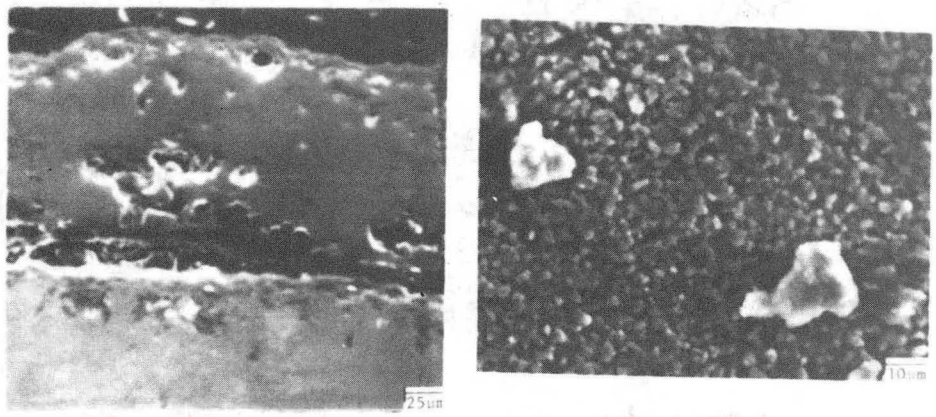

2 1/4 Cr 1 Mo Steel

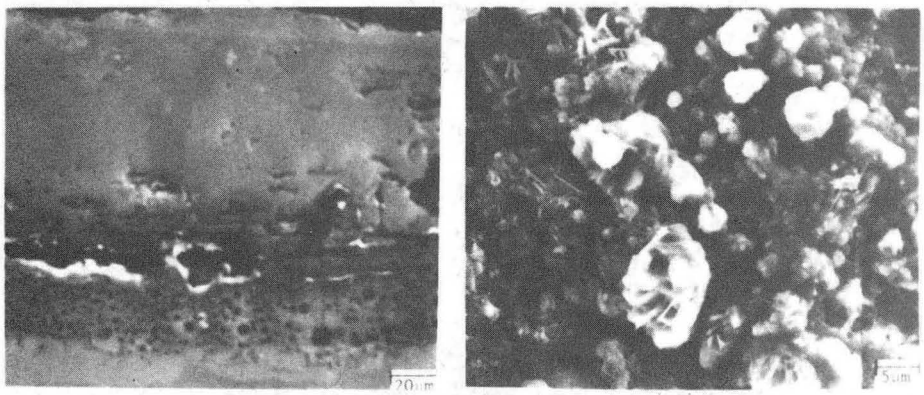

9 Cr 1 Mo Steel

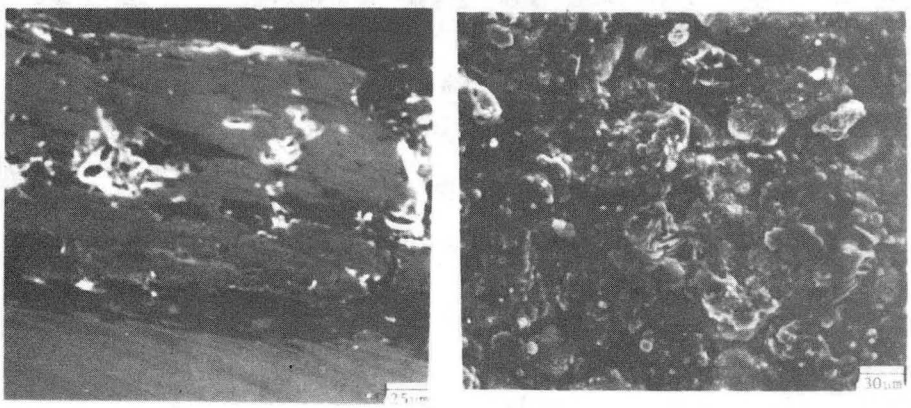

410 SS

Emersion Tester	Temp. =850°C
Erosion-Corrosion	Vel. =15m/s
100μm Al_2O_3	α =45°
Methane air	Time =30min.

Fig. 21. Cross section and surface morphology of scales of 2 1/4, 9 and 12Cr steels eroded-corroded at 850°C using 100μm Al_2O_3.

XBB 841-96

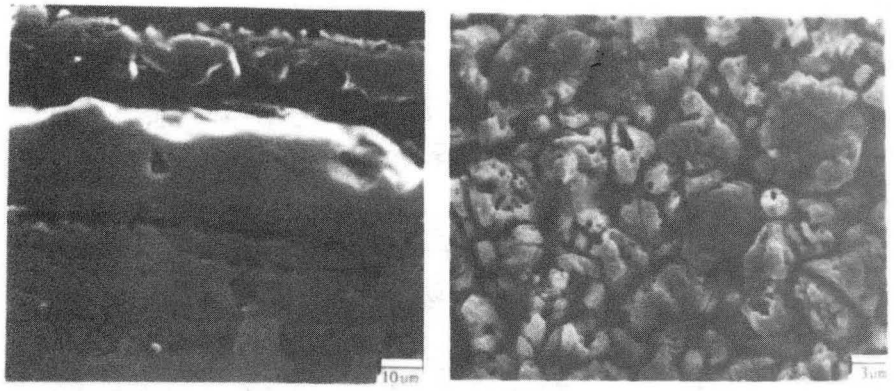

5 Cr 1/2 Mo Steel

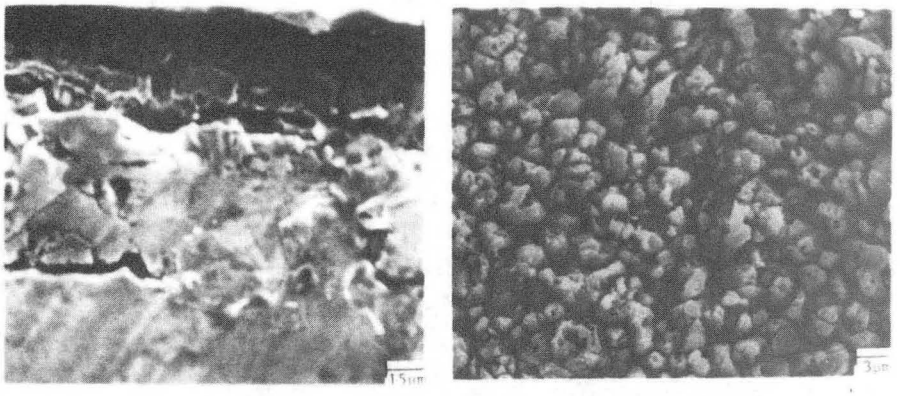

9 Cr 1 Mo Steel

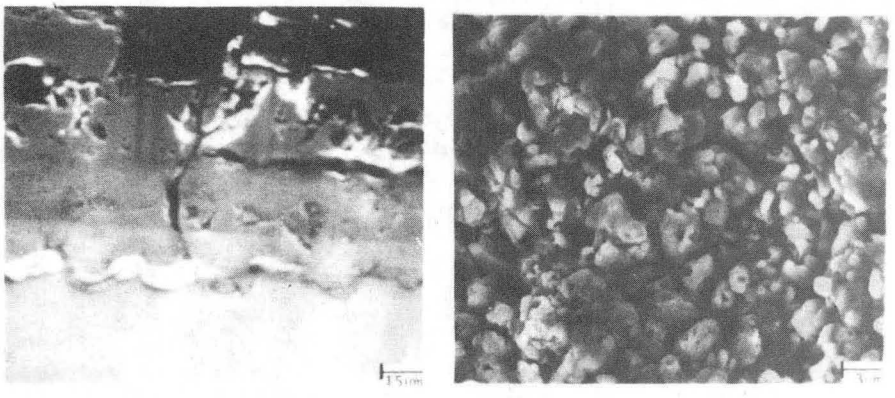

410 SS

Emersion Tester	Temp. =950°C
Erosion-Corrosion	Vel. =15m/s
50μm Al_2O_3	α =45°
Methane air	Time =30min.

Fig. 22. Cross section and surface morphology of scales of 5, 9 and 12Cr steels eroded-corroded at 950°C using 50μm Al_2O_3. XBB 841-105

9 Cr 1 Mo Steel
Temp. =800°C

9 Cr 1 Mo Steel
Temp. =850°C

9 Cr 1 Mo Steel
Temp. =950°C

Emersion Tester
Erosion-Corrosion
100μm Al_2O_3

Methane-air
Vel. = 5m/s
α =45°

Fig.23. Surface morphology of eroded-corroded 9Cr1Mo steel at three different test temperatures using 100μm Al_2O_3.

XBB 841-106

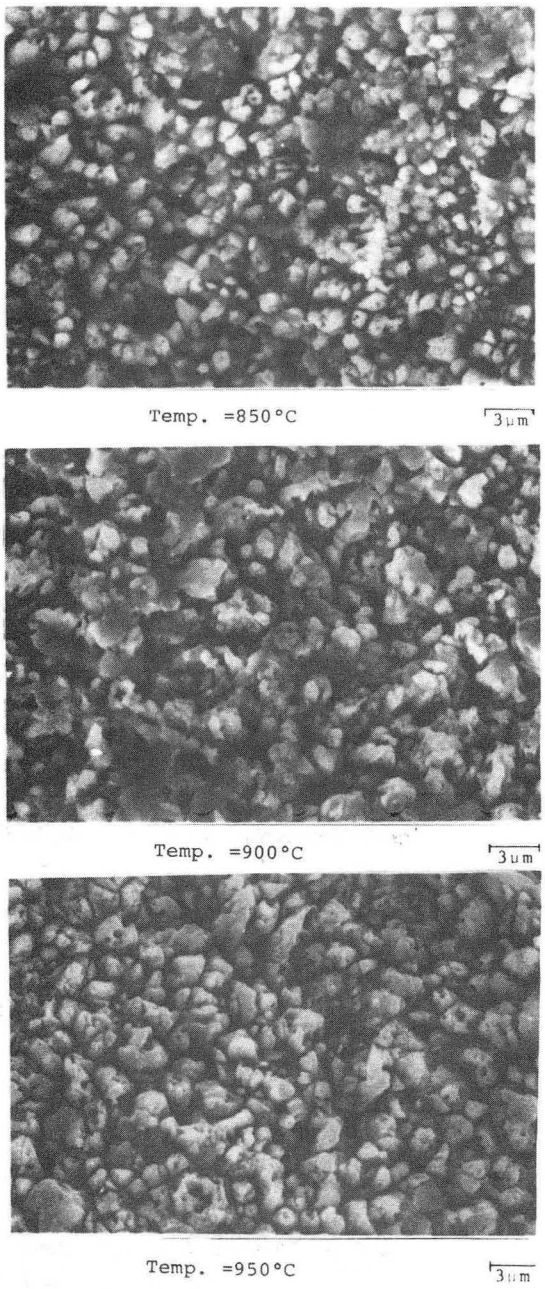

Fig.24. Surface morphology of eroded-corroded 9Cr1Mo steel at three different test temperatures using 50μm Al_2O_3.

XBB 841-104

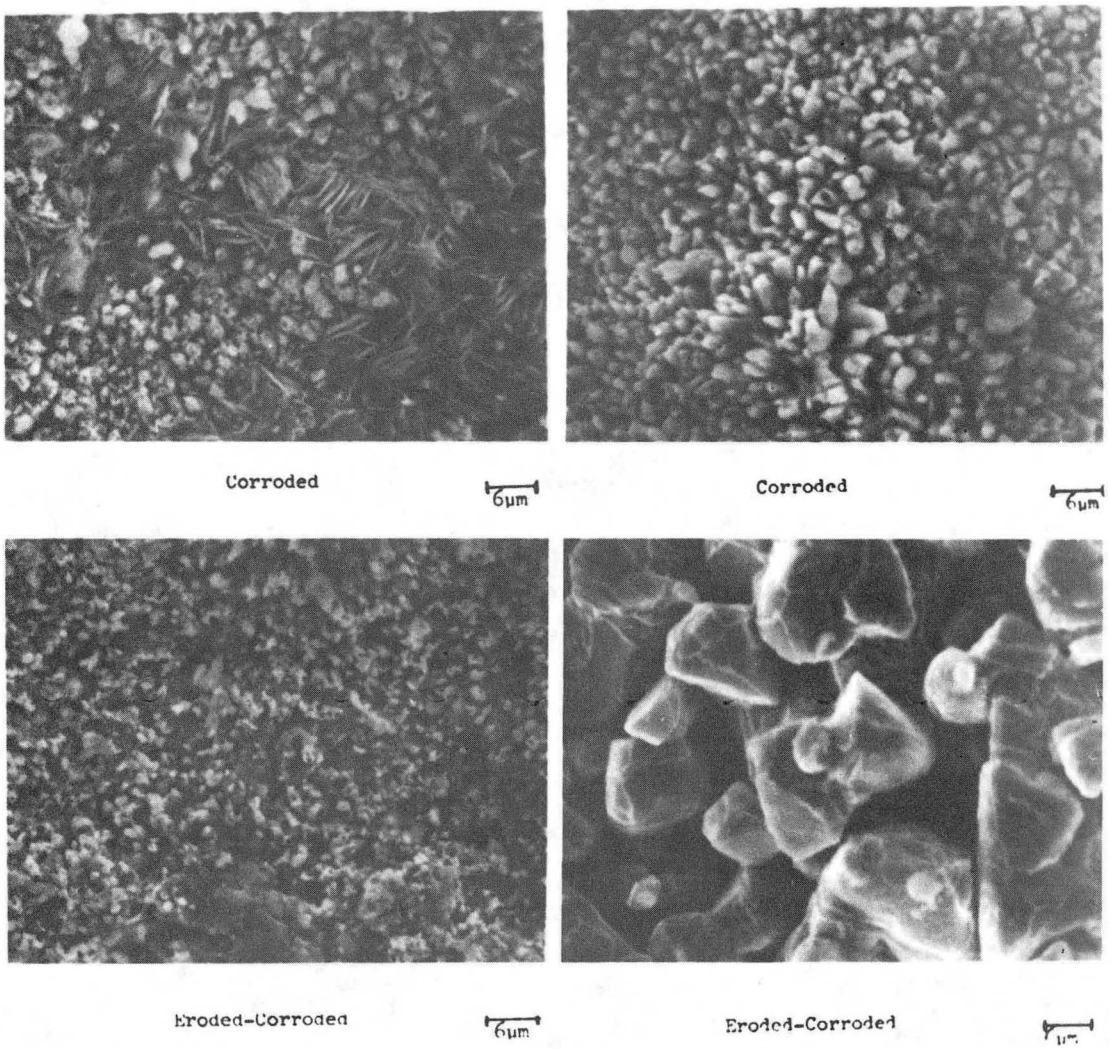

Fig. 25. Surface morphology of eroded-corroded 410SS at two test temperatures using 5μm flyash.

XBB 841-107

DISTRIBUTION LIST

Wate Bakker
EPRI
3214 Hillview Avenue
P.O. Box 10412
Palo Alto, CA 94304

B.R. Banerjee
Ingersoll-Rand Company
P.O. Box 301
Princeton, NJ 08540

K.L. Baumert
Air Products & Chemicals, Inc.
P.O. Box 538
Allentown, PA 18105

S.M. Benford
NASA Lewis Research Center
21000 Brookpark Road
Cleveland, OH 41135

A.E. Biggs
Arco Chemicals
3801 W. Chester Pike
Newtown Square, PA 19073

R. Blickensderfer
Bureau of Mines
P.O. Box 70
Albany, OR 97321

R.A. Bradley, Manager
Fossil Energy Materials Program
Oak Ridge National Laboratory
P.O. Box X
Oak Ridge, TN 37830

Richard Brown
Materials Laboratory
Department of Chemical Engineering
University of Rhode Island
Kingston, RI 02881

DISTRIBUTION LIST cont'd

D.H. Buckley
NASA Lewis Research Center
21000 Brookpark Road
Cleveland, OH 41135

P.T. Carlson, Task Leader
Fossil Energy Materials Program
Oak Ridge National Laboratory
P.O. Box X
Oak Ridge, TN 37830

J. Carpenter
ECUT Program
Oak Ridge National Laboratory
P.O. Box X
Oak Ridge, TN 37830

J.P. Carr
Department of Energy, Office of Fossil Energy
FE-42 Mailstop 3222-GTN
Washington, DC 40525

Hans Conrad
Materials Engineering Department
North Carolina State University
Raleigh, NC 27659

P. Crook
Cabot Corporation
Technology Department
1020 W. Park Avenue
Kokomo, IN 46901

S.J. Dapkunas
Department of Energy, Office of Fossil Energy
Technical Coordination Staff FE-14
Mailstop C-156 GTN
Washington, DC 40525

DOE Technical Information Center
P.O. Box 62
Oak Ridge, TN 37830

W.A. Ellingson
Argonne National Laboratory
9700 South Cass Avenue
Argonne, IL 60439

DISTRIBUTION LIST cont'd

J. Gonzales
GTE
Chemical & Metallurgical Division
Hawes Street
Towanda, PA 18848

A. Hammarsten
Teknikum
P.O. Box 534, S-751 21
Uppsala
SWEDEN

E. Haycock
Westhollow Research Center
Shell Development Company
P.O. Box 1380
Houston, TX 77001

J.M. Hobday
Department of Energy
Morgantown Energy Technology Center
P.O. Box 880
Morgantown, WV 26505

E.E. Hoffman, Manager
National Materials Program
Department of Energy
Oak Ridge Operations
P.O. Box E
Oak Ridge, TN 37830

J.A.C. Humphrey
Mechanical Engineering Department
University of California
Berkeley, CA 94720

I.M. Hutchings
University of Cambridge
Department of Metallurgy
Pembroke Street
Cambridge
ENGLAND

Sven Jansson
Stal-Laval Turbin AB
Finspong S-61220
SWEDEN

DISTRIBUTION LIST cont'd

R.R. Judkins
Fossil Energy Materials Program
Oak Ridge National Laboratory
P.O. Box X
Oak Ridge, TN 37830

James Keiser
Oak Ridge National Laboratory
P.O. Box X
Oak Ridge, TN 37830

M.K. Keshavan
Union Carbide Corporation
Coating Services Department
1500 Polco Street
Indianapolis, IN 46224

T. Kosel
University of Notre Dame
Dept. of Metallurgical Engineering
& Materials Science
Box E
Notre Dame, IN 46556

L. Lanier
FMC-Central Engineering Laboratory
1185 Coleman Avenue
Santa Clara, CA 95052

N.H. MacMillan
Pennsylvania State University
167 Materials Research Laboratory
University Park, PA 16802

P.K. Mehrotra
Kennemetal Inc.
1011 Old Salem Road
Greensburg, PA 15601

Ken Magee
Bingham-Williamette Co.
2800 N.W. Front Avenue
Portland, OR 97219

T. Mitchell
Case Western Reserve University
Department of Metallurgy
Cleveland, OH 44106

DISTRIBUTION LIST cont'd

Fred Pettit
Dept. of Metallurgy & Materials Engineering
University of Pittsburgh
Pittsburgh, PA 15261

R.A. Rapp
Metallurgical Engineering
116 W. 19th Avenue
The Ohio State University
Columbus, OH 43210

D.A. Rigney
Metallurgical Engineering
116 W. 19th Avenue
The Ohio State University
Columbus,OH 43210

A.W. Ruff
Metallurgy Division
National Bureau of Standards
B-266 Materials
Washington, DC 20234

Alberto Sagues
IMMR - University of Kentucky
763 Anderson Hall
Lexington, KY 40506

Gordon Sargent
University of Notre Dame
Dept. of Metallurgical Engineering & Materials Science
Box E
Notre Dame, IN 46556

Paul Shewmon
Dept. of Metallurgical Engineering
116 W. 19th Avenue
Columbus, OH 43210

Gerry Sorell
EXXON Research & Engineering Company
P.O. Box 101
Florham Park, NJ 07932

Carl A. Stearns
Head, High Temperature Chemistry Section
NASA, Lewis Research Center 106-1
21000 Brookpark Road
Cleveland, OH 44135

DISTRIBUTION LIST cont'd

John Stringer
University of California
Lawrence Berkeley Laboratory
Mailstop 62/203
Berkeley, CA 94720

Widen Tabakoff
Dept. of Aerospace Engineering
University of Cincinnati
Cincinnati, OH 45221

Otto Bhattacharyya
IITRI
10 West 35th Street
Chicago, IL 60616

J.J. Wert
Metallurgy Department
Vanderbilt University
P.O. Box 1621, Sta. B
Nashville, TN 37235

J.C. Williams
Dept. of Metallurgy & Materials Science
Carnegie-Mellon University
Schenley Park
Pittsburgh, PA 15213

S. Wolf
Department of Energy
Basic Energy Sciences Office
Division of Materials Sciences
Washington, DC 20545

Ian Wright
Materials Science Division
Battelle Memorial Institute
505 King Avenue
Columbus, OH 43201

C.S. Yust
Metals and Ceramics Division
Oak Ridge National Laboratory
P.O. Box X
Oak Ridge, TN 37830

This report was done with support from the Department of Energy. Any conclusions or opinions expressed in this report represent solely those of the author(s) and not necessarily those of The Regents of the University of California, the Lawrence Berkeley Laboratory or the Department of Energy.

Reference to a company or product name does not imply approval or recommendation of the product by the University of California or the U.S. Department of Energy to the exclusion of others that may be suitable.

LAWRENCE BERKELEY LABORATORY
TECHNICAL INFORMATION DEPARTMENT
UNIVERSITY OF CALIFORNIA
BERKELEY, CALIFORNIA 94720